A GENERALIZED METHOD FOR DETERMINING RADIATION PATTERNS OF APERTURE ANTENNAS AND ITS APPLICATION TO REFLECTOR ANTENNAS

J. Robert Paknys

Technical Report 710964-11

Contract No. NSG 1498

September 1982

National Aeronautics and Space Administration
Langley Research Center
Hampton, Virginia 23665

50272-101

REPORT DOCUMENTATION PAGE	1. REPORT NO.	2.	3. Recipient's Accession No.

4. Title and Subtitle

A GENERALIZED METHOD FOR DETERMINING RADIATION PATTERNS OF APERTURE ANTENNAS AND ITS APPLICATION TO REFLECTOR ANTENNAS

5. Report Date September 1982

6.

7. Author(s)

J. Robert Paknys

8. Performing Organization Rept. No. ESL 711965-11

9. Performing Organization Name and Address

The Ohio State University ElectroScience Laboratory
Department of Electrical Engineering
Columbus, Ohio 43212

10. Project/Task/Work Unit No.

11. Contract(C) or Grant(G) No.

(C)

(G) NSG 1498

12. Sponsoring Organization Name and Address

National Aeronautics and Space Administration
Langley Research Center
Hampton, Virginia 23665

13. Type of Report & Period Covered Technical Report

14.

15. Supplementary Notes

The work reported in this report was also used as a thesis submitted to The Ohio State University Department of Electrical Engineering as part of the requirements for the degree Master of Science.

16. Abstract (Limit: 200 words)

The reflector antenna may be thought of as an aperture antenna. The classical solution for the radiation pattern of such an antenna is found by the "aperture integration" (AI) method. Success with this method depends on how accurately the aperture currents are known beforehand. In the past, geometrical optics (GO) has been employed to find the aperture currents. This approximation is suitable for calculating the main beam and possibly the first few sidelobes.

A better approximation is to use aperture currents calculated from the "Geometrical Theory of Diffraction" (GTD). It will be found that integration of the GTD currents over an extended aperture yields more accurate results for the radiation pattern. This new approach is useful when conventional AI and GTD solutions have no common region of validity. This problem arises in reflector antennas.

Two dimensional models of parabolic reflectors are studied here, however the techniques discussed can be applied to any aperture antenna.

17. Document Analysis a. Descriptors

b. Identifiers/Open-Ended Terms

c. COSATI Field/Group

18. Availability Statement	19. Security Class (This Report) Unclassified	21. No. of Pages 90
	20. Security Class (This Page) Unclassified	22. Price

(See ANSI-Z39.18) *See Instructions on Reverse* OPTIONAL FORM 272 (4-77) (Formerly NTIS-35) Department of Commerce

ACKNOWLEDGMENT

I wish to sincerely thank Professors R.C. Rudduck and W.D. Burnside for their many creative suggestions leading to this thesis.

TABLE OF CONTENTS

LIST OF TABLES

LIST OF FIGURES

FIGURE Page

CHAPTER I

INTRODUCTION

The reflector antenna may be thought of as an aperture antenna. The classical solution for the radiation pattern of such an antenna is found by the "aperture integration" (AI) method. Success with this method depends on how accurately the aperture currents are known beforehand. In the past, geometrical optics (GO) has been employed to find the aperture currents. This approximation is suitable for calculating the main beam and possibly the first few sidelobes.

A better approximation is to use aperture currents calculated from the "Geometrical Theory of Diffraction" (GTD). It will be found that integration of the GTD currents over an extended aperture yields more accurate results for the radiation pattern. In fact, if the plane of integration is extended to infinity, our solution is expected to be exact in a "high frequency sense."

The radiation pattern away from the main beam may alternatively be calculated directly from GTD without any integration. A fundamental limitation of this approach is that it usually fails in the far zone near the reflector axis. One exception,however, is the special case of uniform aperture illumination. Then, GTD may be used to calculate the far field pattern, arbitrarily close to the reflector axis. This solution is exact in a high frequency sense.

Because there exists an "exact" high frequency solution for the far zone radiation pattern of a reflector antenna with a uniform aperture field, this case will be used as a check on the validity of results obtained by: 1) aperture integration of GO currents (which shall be refered to as "AI") and 2) integration of GTD currents over an extended aperture (which shall be called "AIE").

The far field radiation patterns of both offset and non offset reflectors will be examined. All discussions will deal with two dimensional models only. Except for Chapter VIII, it shall also be assumed the feed is a magnetic line source, with or without an amplitude taper. Results for these configurations will reveal that the error introduced by the GO approximation of aperture currents is more serious for an offset reflector than in the non offset case.

In Chapter VI, some general observations are made about the validity of GTD and AI solutions. It is known that evaluation of the radiation integral by the method of stationary phase yields the geometrical optics solution for the reflected field. Also, endpoint contributions to the integral correspond to edge diffracted fields.

Since the GTD solution consists of reflected and edge diffracted rays, one can decide whether or not GTD can be used to find the radiation pattern from examination of the integrand in the AI solution.

A suitable criterion for choosing the limits of integration in a practical application of AIE is discussed in Chapter VII. It will be found that little is gained by integrating the aperture field beyond its GTD transition regions.

Finally, Chapter VIII examines a two dimensional version of the offset reflector treated by Chu and Turrin [5]. In this case, an electric line source feed is used. AI and AIE results are compared with GTD. Effects of varying the limits of integration are also discussed.

CHAPTER II

PRESENT METHODS AND PROBLEMS

The AI solution is limited by the accuracy of geometrical optics used in calculating the aperture currents. Depending on the reflector geometry and feed, the GO current approximation may or may not be acceptable. Our criterion of acceptability here is that the AI and GTD solutions overlap in our region of interest.

One case where the two solutions do not overlap is the offset reflector of Chu and Turrin [5], as shown in Figure 2.1. The AI and GTD solutions, calculated by the NEC reflector code [6] are shown in Figure 2.2. It is important to emphasize that this problem is not unique to the NEC reflector code. Rather, it is a fundamental limitation of the AI and GTD solutions.

In general, the far out sidelobes calculated by AI tend to be too low. On the basis of GTD considerations, a modified obliquity factor for the AI radiation integral has been derived by Rudduck [7]. This factor improves the AI sidelobe levels considerably, and is used in the reflector code. However, in an offset reflector, the sidelobes

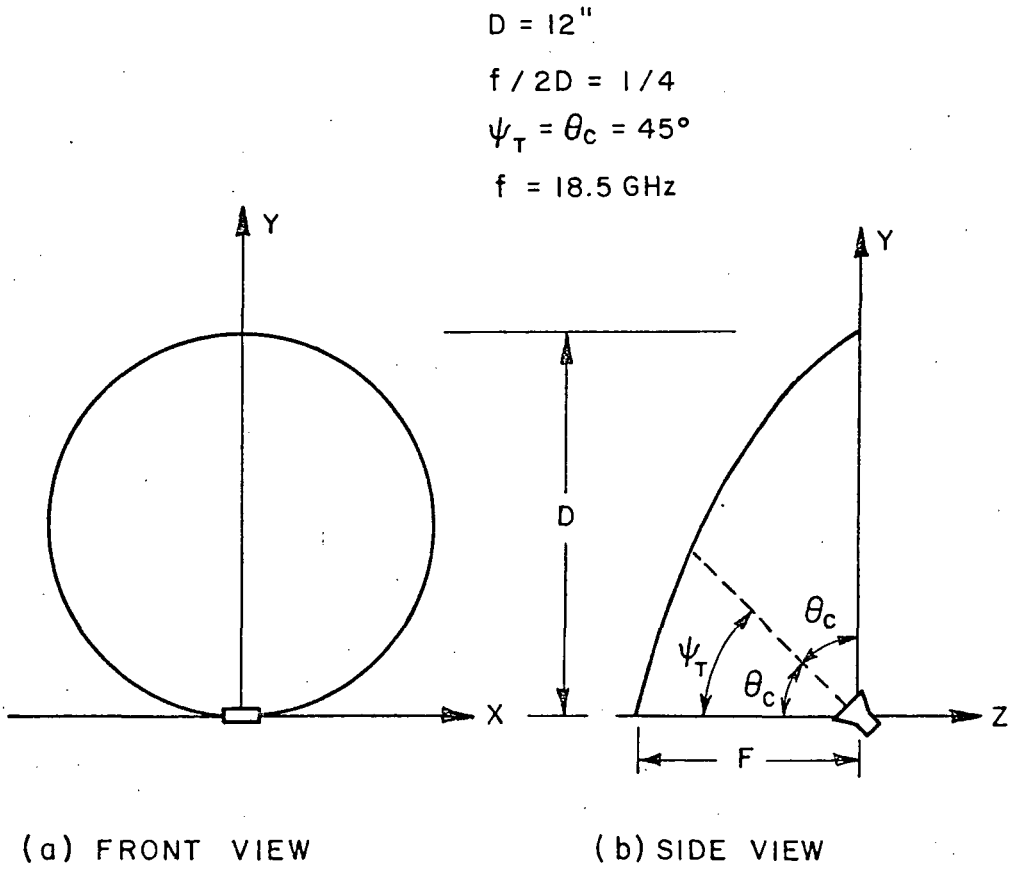

Figure 2.1 Offset reflector of Chu and Turrin (from [5]).

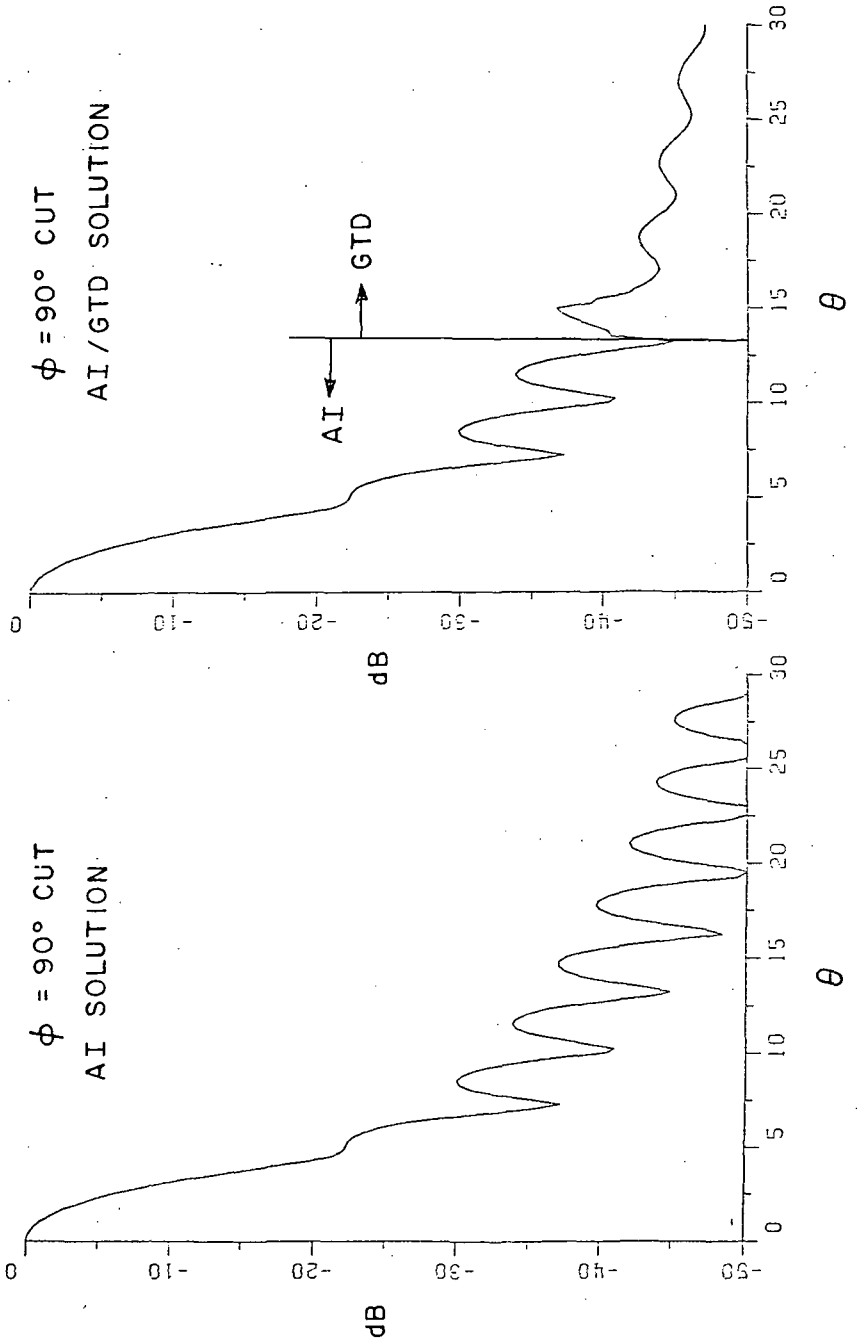

Figure 2.2 AI and GTD far field radiation patterns calculated for the offset reflector of Chu and Turrin.

calculated by AI tend to be too low, and also in the wrong position. This cannot be corrected by a simple factor.

This problem motivates a preliminary study of an offset reflector in two dimensions. In particular, we will find that the GO current approximation is not always adequate.

CHAPTER III

APERTURE FIELD METHOD

This chapter begins with a discussion of the aperture field method. It is well known [1] that the unique solution requires knowledge of currents over an aperture plane of infinite extent. For illustrative purposes, we calculate the far field patterns of offset and non offset reflectors illuminated by a magnetic line source. These patterns are found by integrating aperture currents derived from the geometrical optics (GO) approximation. The results are also compared with solutions that are known to be exact in a high frequency sense. Errors in the solution are attributed to the GO current approximation.

These errors motivate a search for a more accurate representation of the aperture currents. We shall use currents calculated by GTD, and integrate them over a greater extent of the aperture plane. The result is closer agreement with the exact solution. This is to be expected, in light of the uniqueness theorem for electromagnetic fields [1].

A. RADIATION INTEGRALS

We seek the solution for the electromagnetic field problem in two dimensions, as in Figure 3.1. By the uniqueness theorem [1], a solution inside the region Λ, bounded by the perimeter σ is uniquely determined by:

(1) the impressed electric and magnetic currents $\overline{J}(\overline{\rho}')$, and $\overline{M}(\overline{\rho}')$ inside Λ

and

(2) the surface electric and magnetic currents $\hat{n} \times \overline{H}(\overline{\rho}')$ and $\overline{E}(\overline{\rho}') \times \hat{n}$ on σ.

We choose to neglect direct radiation from the feed. Then the solution is completely determined by the surface currents on σ_1 and σ_2. Furthermore, from the Sommerfeld radiation condition, we argue that the currents on σ_2 do not contribute as $\rho_a \to \infty$. This reduces the problem to finding the currents on the "aperture plane" σ_1. These currents follow from

$$\overline{M}_a(y) = \overline{E}(y) \times \hat{n} \quad , \text{ and}$$

$$\overline{J}_a(y) = \hat{n} \times \overline{H}(y) \quad .$$

The problem may be simplified further through the use of image theory. Since we are only interested in the solution for $x > 0$, a perfect conductor of magnetism may be introduced just to the left of σ_1. This shorts out the magnetic current, and doubles the electric current:

$$\bar{J}_a(y) = 2\hat{n} \times \bar{H}(y) \text{ , and}$$
$$\bar{M}_a(y) = 0 \quad . \tag{3.1}$$

An equally valid alternative representation results if an electric conductor is introduced instead. Similar reasoning yields

$$\bar{J}_a(y) = 0 \text{ , and}$$
$$\bar{M}_a(y) = 2\bar{E}(y) \times \hat{n} \quad . \tag{3.2}$$

Except for Chapter VIII, all our investigations use a magnetic line source for illumination. The equations for an electric line source are easily obtained by duality, and will not be discussed.

In our case, $\bar{H}(y)$ is always $\hat{z}$ directed. Using Equation (3.1), we see $\bar{J}(y)$ will be $\hat{y}$ directed:

$$\hat{y}J_a(y) = -\hat{y}2H_z(y) \ .$$

For a $\hat{y}$ directed current as in Figure 3.2, the appropriate radiation integral is (Appendix A)

$$H_z(\bar{\rho}) = \sqrt{\frac{jk}{8\pi}} \int_{-\infty}^{\infty} \hat{z} \cdot (\hat{y} \times \hat{\rho}_o) \cdot (-2H_z(y')) \frac{e^{-jk\rho_o}}{\sqrt{\rho_o}} \, dy' \tag{3.3}$$

with

$$\rho_o = |\bar{\rho} - \bar{\rho}'| = |\bar{\rho} - \bar{y}'|$$

where a prime denotes the variable of integration. From Figure 3.2, we see see that

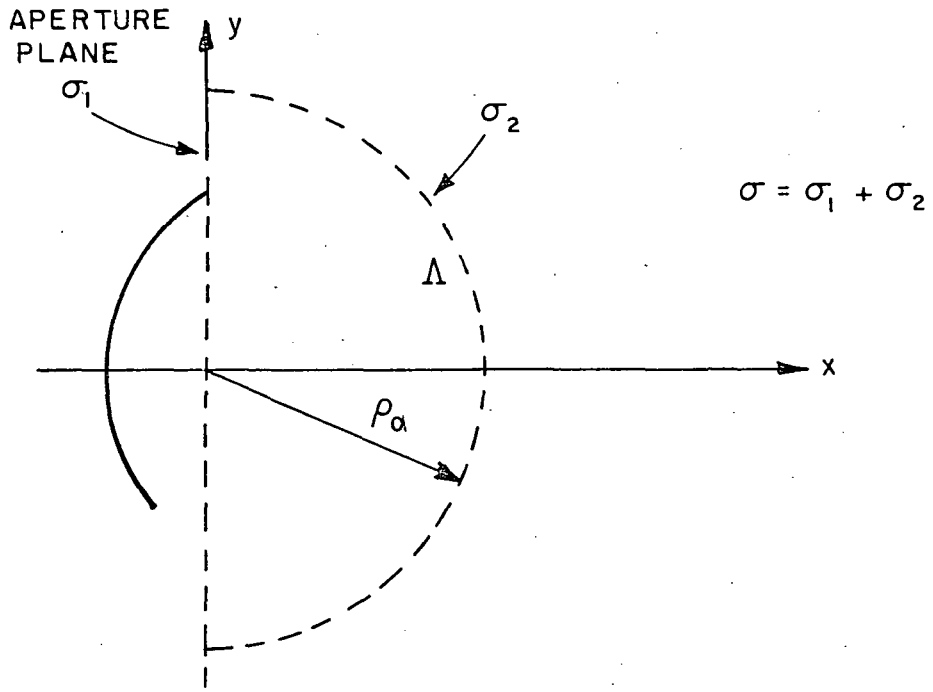

Figure 3.1 Surfaces used in applying the uniqueness theorem and equivalence principle.

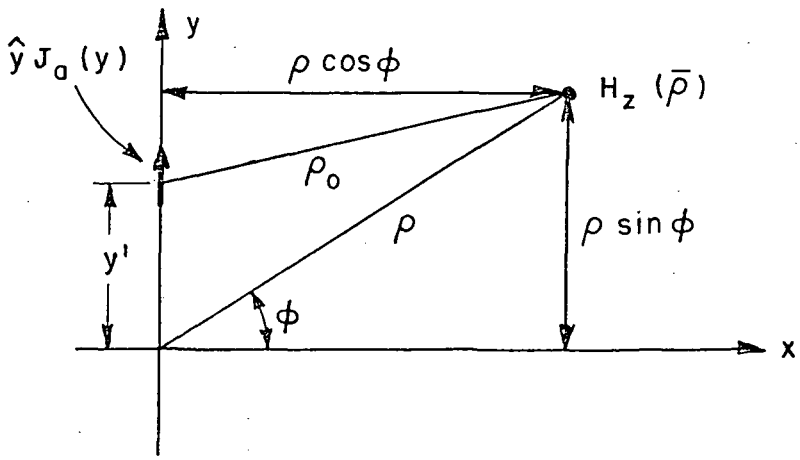

Figure 3.2 A $\hat{y}$ directed electric current.

$$\rho_o^2 = (\rho \cos\phi)^2 + (\rho \sin\phi - y')^2$$
$$= \rho^2 + y'^2 - 2\rho y' \sin\phi$$

so that the general expression for the near field radiation integral with a magnetic line source becomes†

$$H_z(\bar{\rho}) = \sqrt{\frac{jk}{8\pi}}\, 2\cos\phi \int_{-\infty}^{\infty} \frac{\rho}{\rho_o}\, H_z(y')\, \frac{e^{-jk\rho_o}}{\sqrt{\rho_o}}\, dy' \quad . \tag{3.4}$$

This expression may be simplified for the far field. With $\bar{\rho}$ and $\bar{\rho}_o$ parallel,

$$\rho_o = \rho - y' \sin\phi \qquad \text{and}$$

$$\hat{z} \cdot (\hat{y} \times \hat{\rho}_o) = -\cos\phi$$

so that the far field radiation pattern may be found from

$$H_z(\bar{\rho}) = \frac{e^{-jk\rho}}{\sqrt{\rho}} \sqrt{\frac{jk}{8\pi}}\, 2\cos\phi \int_{-\infty}^{\infty} H_z(y')\, e^{jky'\sin\phi}\, dy' \quad . \tag{3.5}$$

The remaining problem is to find the aperture field. The following two chapters shall examine two approximations for the aperture field: GO and GTD.

---

†It has been suggested by Rudduck [7] that the $\cos\phi$ obliquity factor can be replaced by $\cos(\phi/2)$ if the aperture fields are found by geometrical optics.

CHAPTER IV

APERTURE INTEGRATION WITH G.O. CURRENTS

As a first approximation, we now use GO to find the aperture field. We shall refer to the solution obtained by integrating GO fields as "AI" (for aperture integration).

When discussing the GO rays, we shall take the origin of coordinates as the parabola vertex - however, it will be more convenient to redefine the y axis as the aperture plane when carrying out the integration.

A. CALCULATION OF GO APERTURE FIELDS

The general method of GO is outlined in Appendix B, and the geometry relevant to our problem is in Figure 4.1.

For a parabolic surface with its focus at f,

$$x = y^2/4f \quad .$$

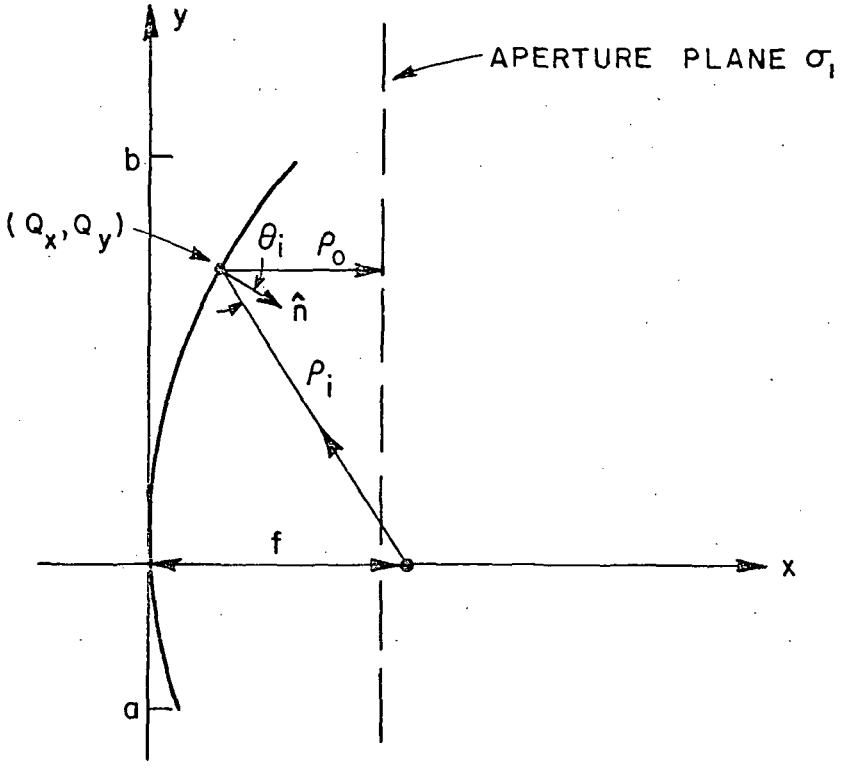

Figure 4.1 Geometry for calculation of GO aperture fields.

The radius of curvature R_c at the reflection point (Q_x,Q_y) is given by

$$|R_c| = \frac{[1 + (d_x/d_y)^2]^{3/2}}{d^2x/dy^2} \quad .$$

In particular, for a parabola,

$$R_c = -2f\,[1 + (Q_y/2f)^2]^{3/2} \quad .$$

From this, we calculate the caustic distance ρ^r for the reflected field

$$\frac{1}{\rho^r} = \frac{1}{\rho_o{}'} + \frac{2}{R_c \cos\theta^i} \quad .$$

For the special case when the source is at the focus, $x_s = f$,

$$R_c = -2f \sec^3(\alpha/2) \ ,$$

$$\cos\theta^i = \cos \alpha/2 \quad , \text{ and}$$

$$\rho_o{}' = f \sec^2 \alpha/2 \ ,$$

so that $\rho^r \to \infty$. This means the image for the reflected field appears to be at infinity. Equivalently, the reflected field is a plane wave. The spreading factor is

$$A(\rho_o) = \sqrt{\frac{\rho^r}{\rho_r + \rho_o}}$$

When $x_s = f$, we see $A(\rho_o) = 1$.

The reflected field with magnetic line source illumination is given by

$$\bar{H}^{refl} = \hat{z}\, H^{inc}(Q_R) R_h\, A(\rho_o) e^{-jk\rho_o} \quad ,$$

where $R_h = 1$ is the reflection coefficient. For our case of a focussed parabola, we find that

$$\bar{H}^{refl} = \hat{z}\, H^{inc}(Q_R) e^{-jk\rho_o} \quad .$$

Let us assume that the magnetic line source has as its field

$$\bar{H}^{inc} = \hat{z}\, \frac{e^{-jk\rho_i}}{\sqrt{\rho_i}} \quad . \tag{4.1}$$

The GO aperture field then follows from

$$\bar{H}^{refl} = \hat{z}\, \frac{e^{-jk(\rho_i+\rho_o)}}{\sqrt{\rho_i}} \quad . \tag{4.2}$$

If f/D is greater than 1/2, we may neglect the $1/\sqrt{\rho_i}$ amplitude taper of the aperture field. Then (4.2) may be reduced to

$$\bar{H}^{refl} \approx \hat{z}\, \frac{e^{-jk(\rho_i+\rho_o)}}{\sqrt{f}} \tag{4.3}$$

with ρ_i and ρ_o as in Figure 4.1. We shall use (4.3) for the aperture field $H_z(y')$, in (3.5) to determine far field radiation patterns for the offset and non offset reflectors of Figure 4.2.

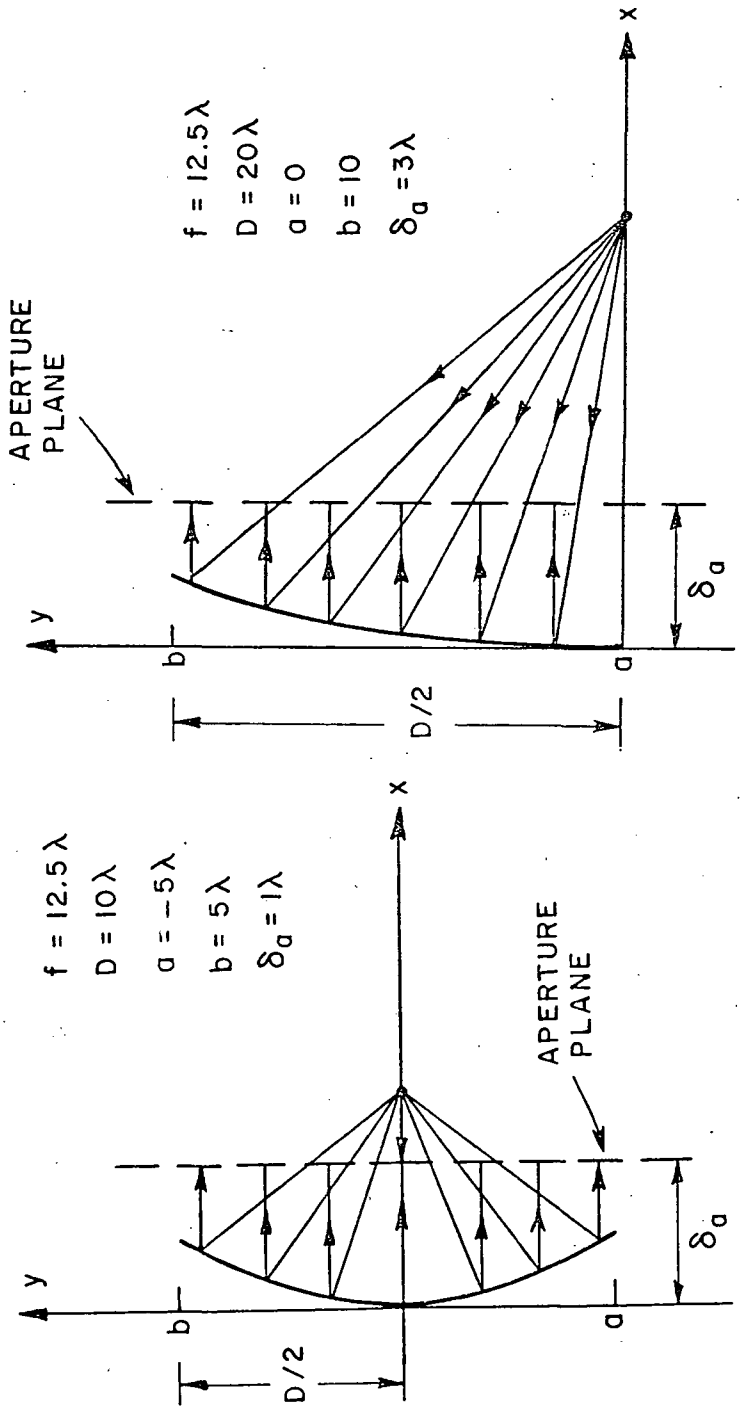

Figure 4.2 Offset and non offset reflectors.

B. INTEGRATION OF THE CURRENT

Noting that $\rho_i + \rho_o$ of Figure 4.1 is constant, the far field radiation pattern follows from Equations (4.3) and (3.5):

$$H_z(\bar{\rho}) = \frac{e^{-jk\rho}}{\sqrt{\rho}} \sqrt{\frac{jk}{8\pi}}\ 2\cos\phi\ I(\phi)\ , \tag{4.4}$$

where

$$I(\phi) \equiv \frac{e^{-jk(\rho_i+\rho_o)}}{\sqrt{f}} \int_a^b e^{jky'\sin\phi}\, dy'$$

$$= \frac{e^{-jk(\rho_i+\rho_o)}}{\sqrt{f}}\ 2e^{jk[(a+b)/2]\sin\phi}\ \frac{\sin(k[(b-a)/2]\sin\phi)}{k\sin\phi}\ .$$

For the magnitude of the pattern, we see that

$$|H_z| \propto \cos\phi\ \frac{\sin(k[(b-a)/2]\sin\phi)}{\sin\phi}$$

This is the same for either the offset or non offset cases! The GO approximation for the aperture currents has failed to predict any differences in the radiation patterns. This motivates a search for a more accurate approximation of the aperture currents. In the next chapter, we shall use aperture fields calculated by GTD.

CHAPTER V

EXTENDED APERTURE INTEGRATION (AIE) WITH GTD CURRENTS

In the previous chapter, we saw that GO was inadequate in modelling the difference between aperture fields of offset and non offset reflectors. In this chapter, we use the next best approximation--GTD, to find the aperture fields. The field will be smooth and continuous across the entire aperture, and nonzero outside the reflector rim. The radiation integrals will be done numerically. Since the integration extends beyond the reflector rim, we shall call this technique "extended aperture integration"(AIE).

A. CALCULATION OF THE APERTURE FIELDS BY GTD

The details of applying GTD to calculate the aperture fields for the reflectors of Figure 4.2 are first described.

The general geometry is shown in Figure 5.1. The field at (x,y) has three contributions: the reflected ray, as calculated by GO in the previous section, plus two edge diffracted rays which compensate for

discontinuities in the GO field. Higher order effects such as doubly diffracted rays from Q_{e1} to Q_{e2} are neglected in this analysis. Shadowing effects of the edges are also neglected.

The general form of the GTD solution is discussed in Appendix C. The details for our particular application are disclosed in the following sections.

B. EDGE DIFFRACTED FIELDS

The procedure for calculating the diffracted field is the same for both edges. Let us consider the upper edge of Figure 5.1. The incident field L parameters are given by

$$L^{io} = L^{in} = \frac{\rho'_1 \rho_1}{\rho'_1 + \rho_1} \quad .$$

The reflected field L parameters depend on the reflected field caustic distance at the edge ρ_1^{re}. To properly compensate for a discontinuity in the reflection from the "o" face,

$$L^{ro} = \frac{\rho_1^{re} \rho_1}{\rho_1^{re} + \rho_1} \quad ,$$

where ρ_1^{re} is constant and is given by

$$\rho_1^{re} = \rho_1^{r} \, (Q_R = Q_{e1}) \quad .$$

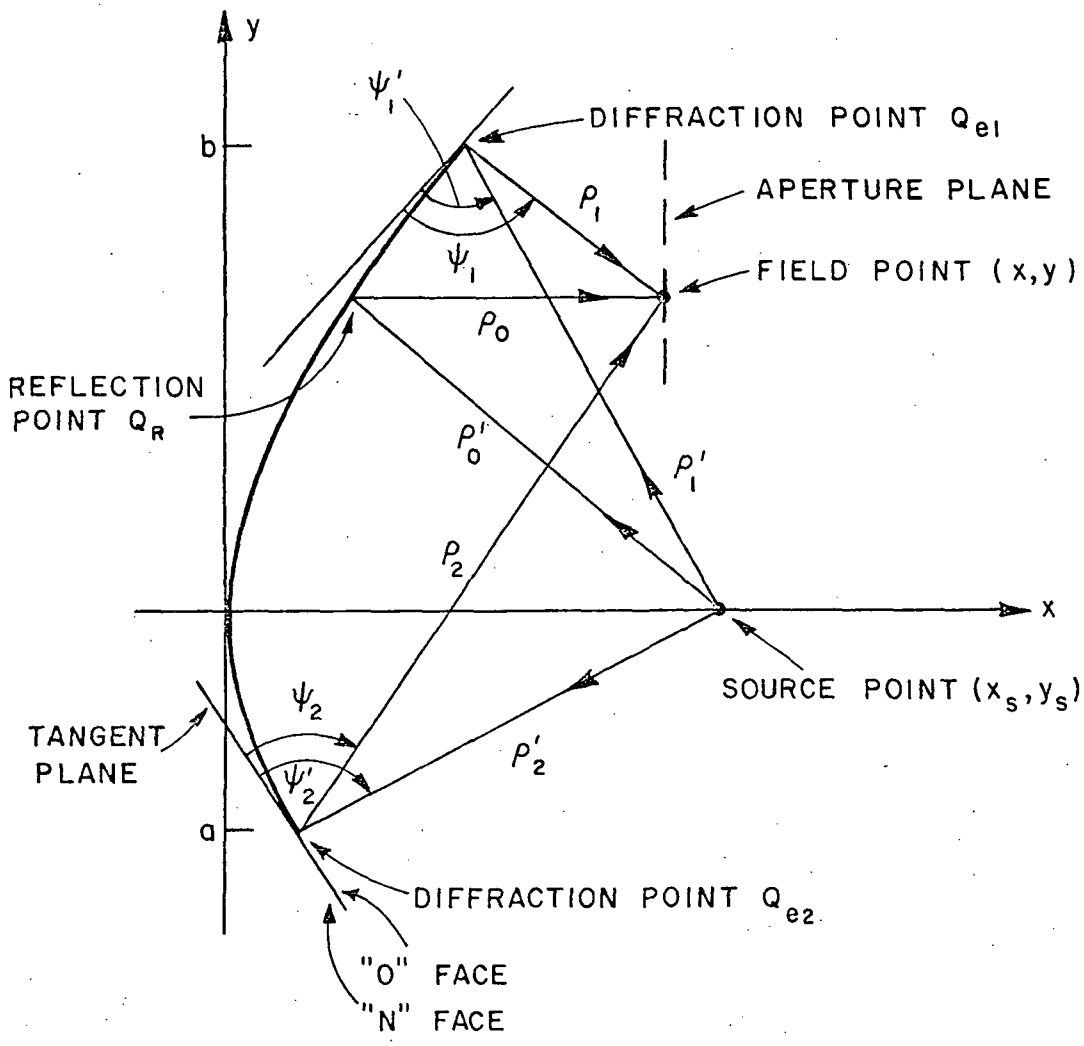

Figure 5.1. Geometry for the GTD near field solution.

Since we are dealing with a focussed parabola, $\sigma_1^{re \to \infty}$ so that

$$L^{ro} = \frac{\rho_1}{1 + \rho_1/\rho_1^{re}} = \rho_1$$

The field point never approaches the "n" face reflection boundary, so we may safely neglect its curvature. Approximating it as a flat surface,

$$L^{rn} \approx \frac{\rho_1' \rho_1}{\rho_1' + \rho_1}$$

Since n=2 for the half plane edge, it follows that

$$a(\psi_1 \pm \psi_1') = 2\cos^2\left(\frac{\psi_1 \pm \psi_1'}{2}\right) \quad .$$

This completes the description of all the necessary parameters for the diffraction coefficient for Q_{e1}. The spreading factor for this diffracted ray is given by

$$A(\rho_1) = \frac{1}{\sqrt{\rho_1}} \quad .$$

For our case of magnetic line source illumination, the field diffracted from edge Q_{e1} is then given by

$$\bar{H}^{d1} = \hat{z}\, H^i(Q_{e1})\, Dh_1\, A(\rho_1)\, e^{-jk\rho_1} \quad , \text{ or}$$

$$\bar{H}^{d1} = \hat{z}\, \frac{e^{-jk\rho_1'}}{\sqrt{\rho_1'}}\, Dh_1\, \frac{e^{-jk\rho_1}}{\sqrt{\rho_1}} \quad . \tag{5.1}$$

Similarly, for Q_{e2},

$$\overline{H}^{d2} = \hat{z} \frac{e^{-jk\rho_2'}}{\sqrt{\rho_2'}} \quad Dh_2 \frac{e^{-jk\rho_2}}{\sqrt{\rho_2}} \quad . \tag{5.2}$$

The total GTD aperture field is the sum of Equations (4.2), (5.1), and (5.2):

$$\overline{H}(y) = \begin{cases} \overline{H}^{refl} + \overline{H}^{d1} + \overline{H}^{d2} & a \leq y \leq b \\ \overline{H}^{d1} + \overline{H}^{d2} & \text{elsewhere} \end{cases} \quad . \tag{5.3}$$

The G.O. (4.2) and GTD (5.3) aperture fields have been plotted in Figure 5.2 and Figure 5.5 for the non offset and offset reflectors of Figure 4.2.

It is easy enough to integrate the GO aperture field analytically, as was shown in Chapter IV, however, numerical integration must be used to integrate the GTD fields. Resulting radiation patterns for the non offset reflector of Figure 4.2 are shown in Figure 5.3 and Figure 5.4. We see that AI correctly predicts the main beam and first few sidelobes. The results from integrating over an extended aperture (AIE) on $-10 \leq y \leq 10$ is even better. This is to be expected, in light of the uniqueness theorem. In fact, if the integration was carried over an infinite aperture plane, we would expect the AIE and exact solutions to coincide.

We repeat the analysis for the offset reflector of Figure 4.2. The aperture fields are shown in Figure 5.5. The resulting radiation patterns are shown in Figure 5.6 and Figure 5.7. In this case, only the first sidelobe can be found from the AI solution. Again, we see that

the AIE solution provides significant improvement over A.I., in the first few sidelobes. Their magnitude, as well as position are closer to the correct result.

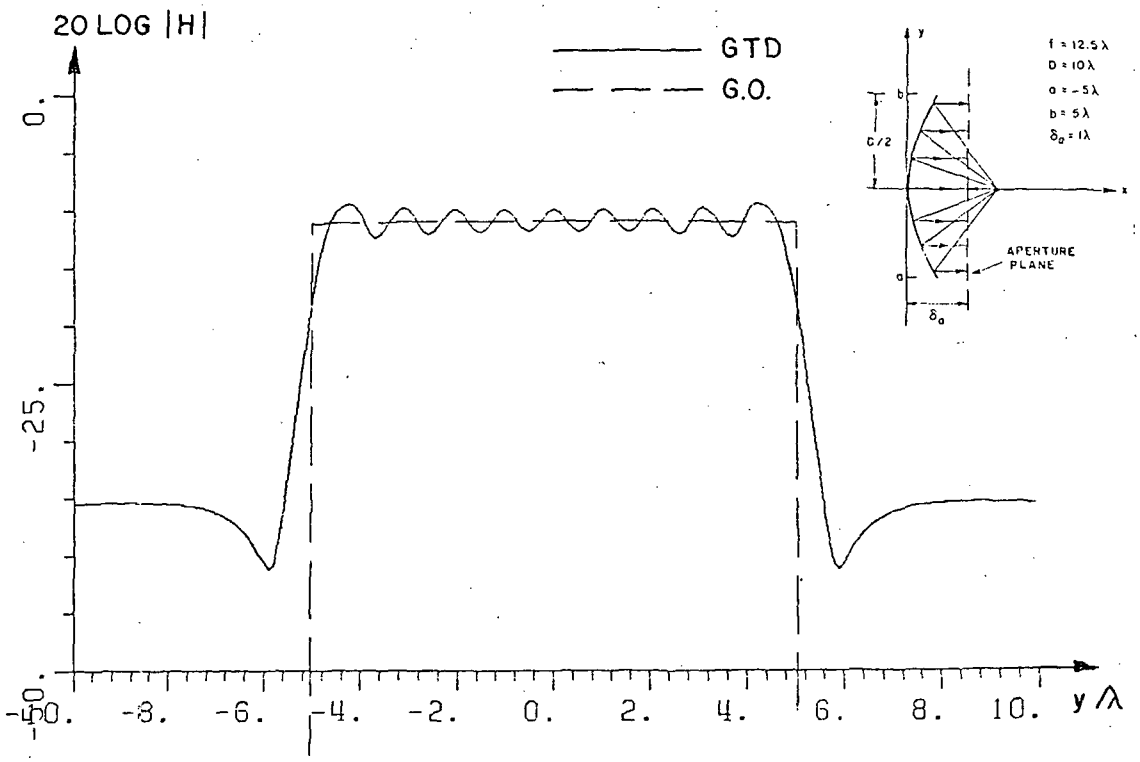

Figure 5.2 Aperture fields for the non offset reflector with magnetic line source illumination.

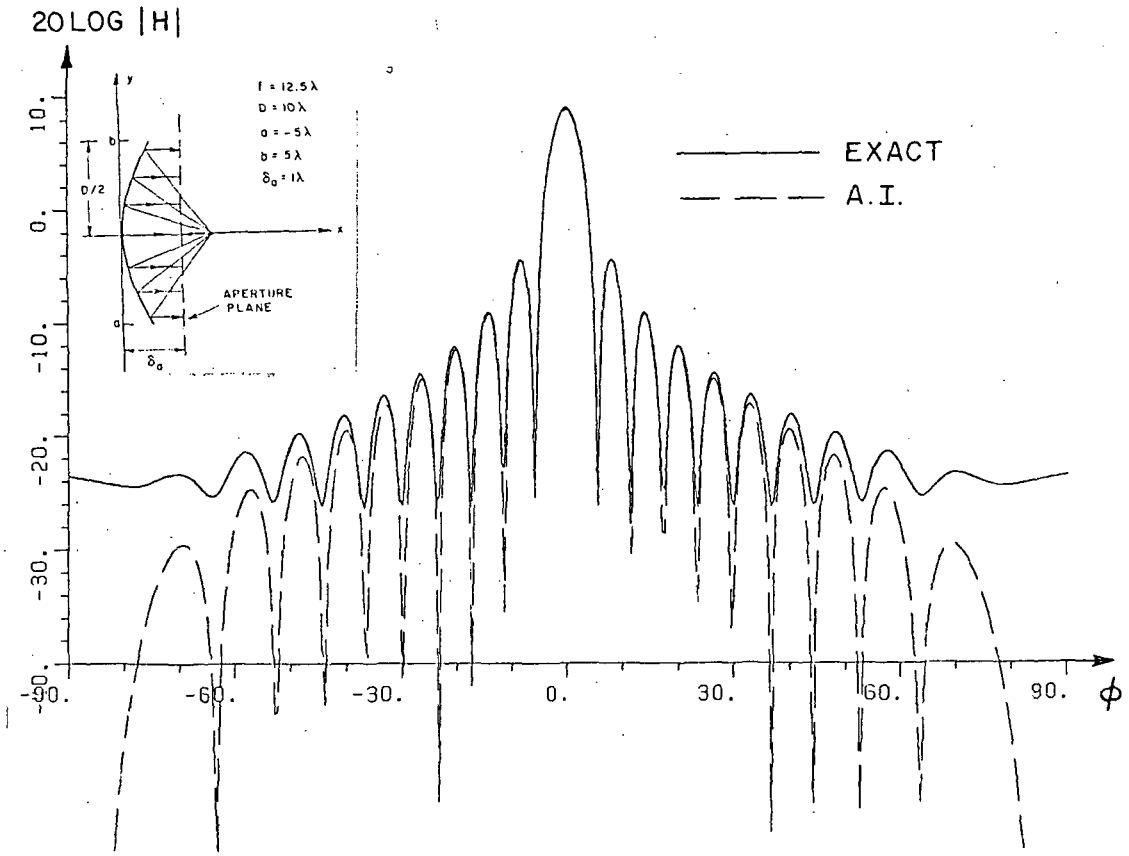

Figure 5.3 Far field radiation pattern for the non offset reflector with uniform illumination. AI solution.

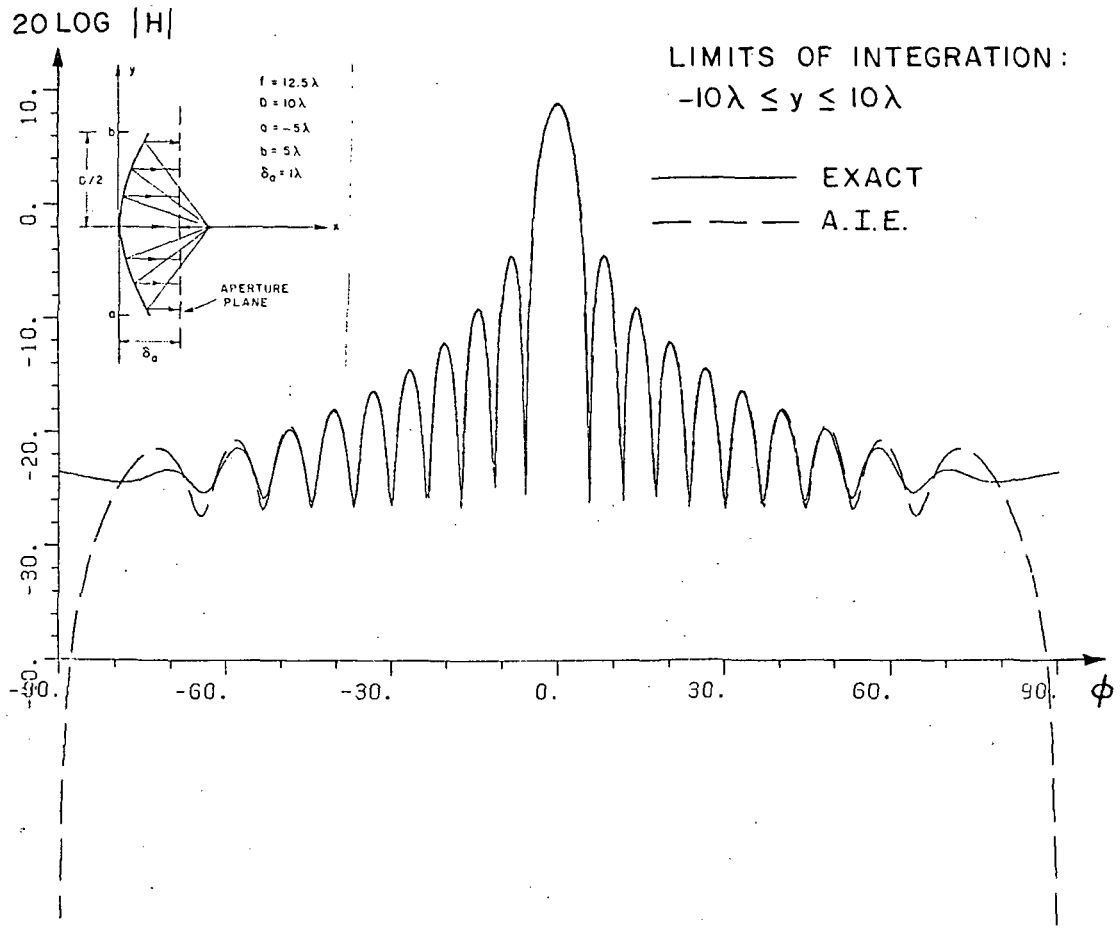

Figure 5.4 Far field radiation pattern for the non offset reflector with uniform illumination. AIE solution.

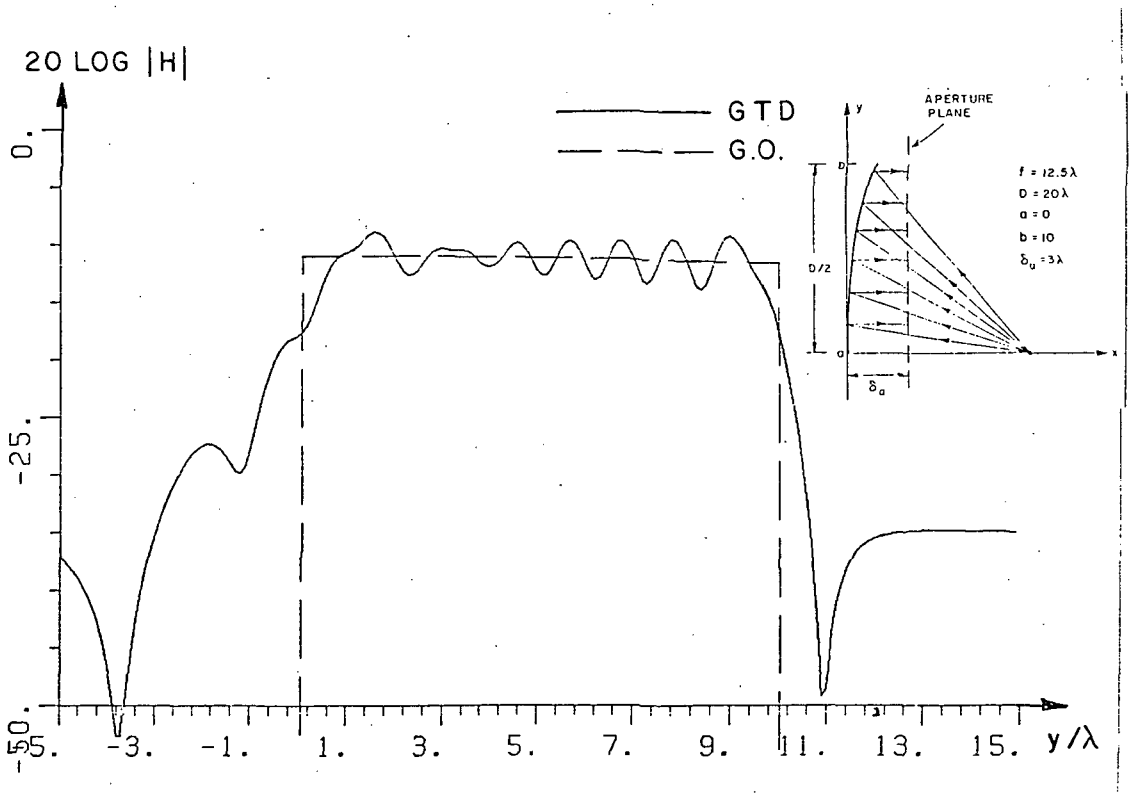

Figure 5.5 Aperture fields for the offset reflector with magnetic line source illumination.

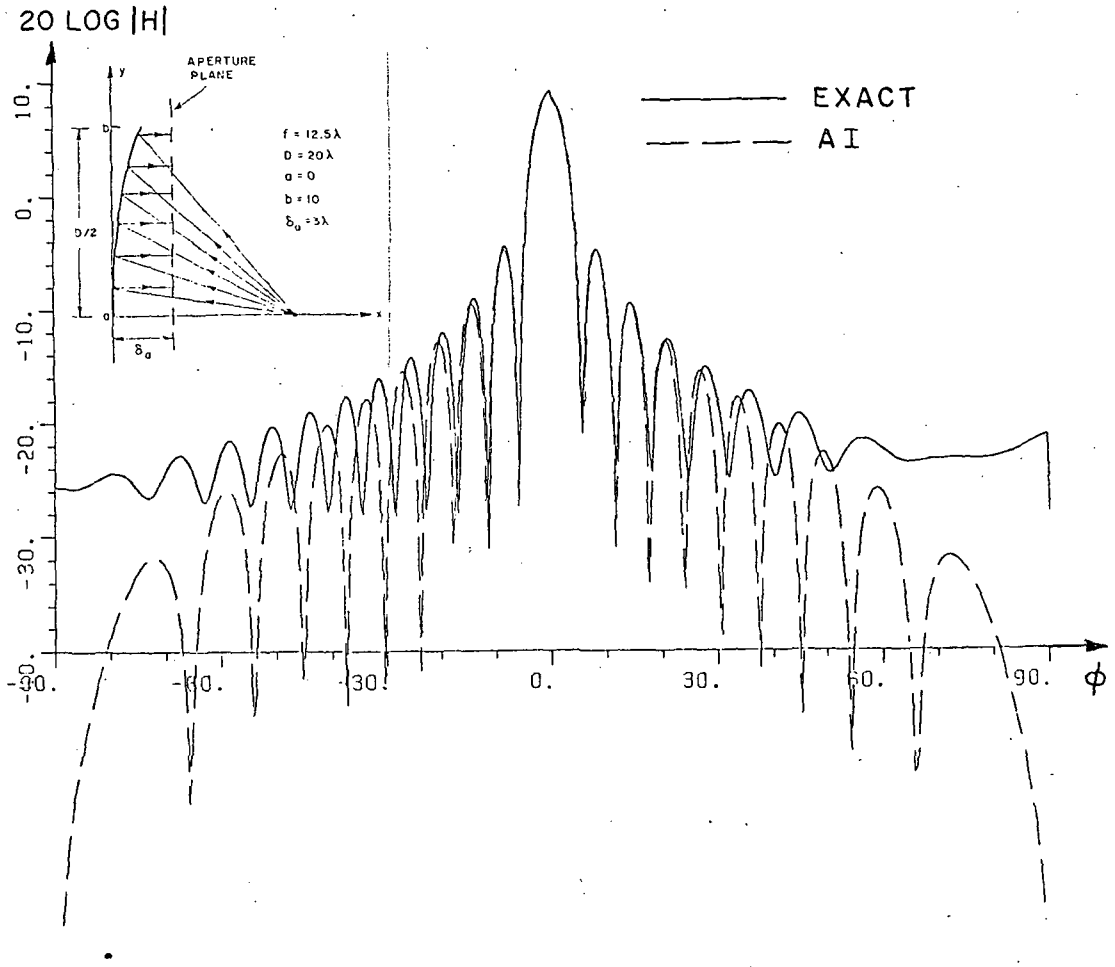

Figure 5.6 Far field radiation pattern for the offset reflector. AI solution.

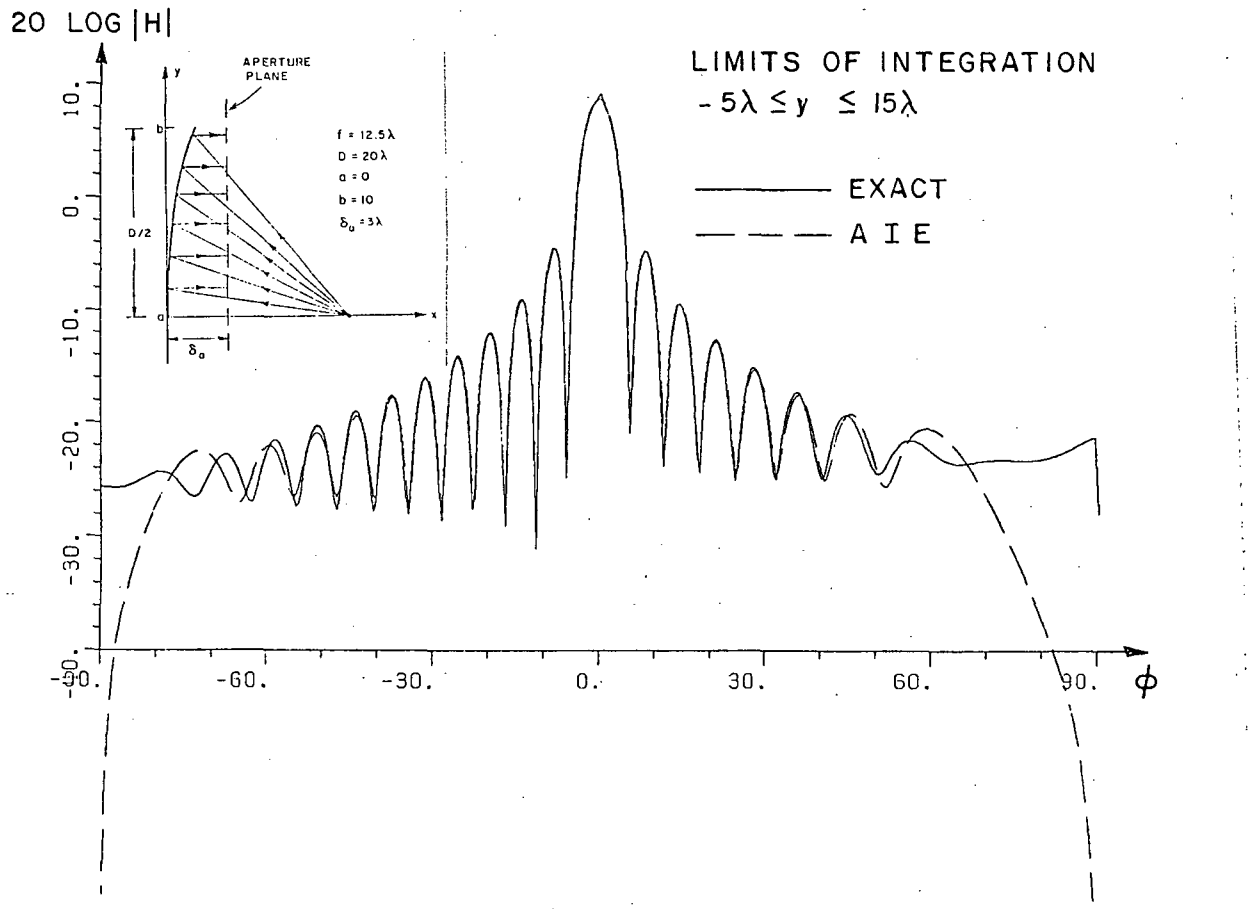

Figure 5.7 Far field radiation pattern for the offset reflector. AIE solution.

CHAPTER VI

GENERAL VALIDITY OF THE GTD SOLUTION

So far, we have only used GTD to calculate the antenna aperture fields. It turns out that we need not be so restrictive. GTD can be used to calculate the field anywhere except at and near "caustics". A caustic is a confluence of rays. Several examples are shown in Figure 6.1.

The advantage of this solution is that no integration is required. The reflected plus edge diffracted rays constitute the entire solution.

In this chapter, we shall restrict our attention to the non offset parabola of Figure 4.2 In this case, we may use GTD to calculate the radiation pattern anywhere except in the far zone near the reflector axis, where the parallel rays meet, i.e., a caustic. We now ask: How close to a caustic does our solution remain valid?

For a focussed parabola, the x axis at infinity is always a caustic, however we shall find that the extent of the caustic region depends on the amplitude taper of the aperture field. In particular,

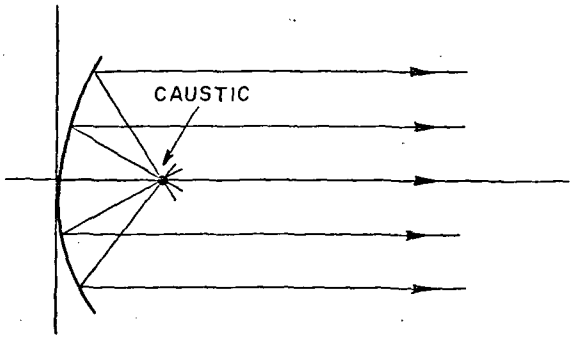

PARABOLIC REFLECTOR

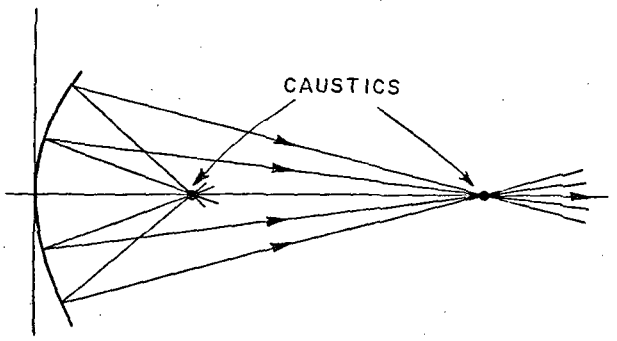

ELLIPTICAL REFLECTOR

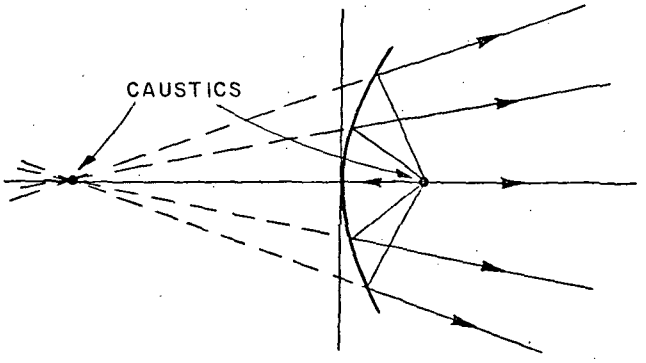

HYPERBOLIC REFLECTOR

Figure 6.1 Examples of caustics.

we shall find that if the aperture field is constant, the extent of the caustic region is infinitesimal. Consequently, in the far zone, the field point may come arbitrarily close to the x axis. This is the origin of the "exact" solution referred to in previous chapters.

When using GTD to calculate aperture currents along σ_1 of Figure 3.1, no problem arose because the field point is deep into the near zone, far away from the caustic.

For a complete discussion, we shall examine near and far field patterns for the non offset reflector of Figure 4.2, with and without a feed amplitude taper. As before, a magnetic line source feed is used throughout. The "nonuniform" aperture field taper used is "parabolic squared" on a pedestal, down 10 dB at the reflector edge.

A. FAR FIELD GTD AND AI SOLUTIONS WITH A UNIFORM APERTURE FIELD

Let us now consider the GTD solution for the reflector in Figure 6.2 with the field point at infinity, making an angle ϕ with respect to the x axis. The reflected ray is always parallel to the x axis, unlike the diffracted rays which may point in any direction. We see that for $\phi \neq 0$, the reflected ray does not contribute to the far field solution. Only the two edge diffracted rays are needed!

It may seem unreasonable that the far field pattern is only dependent on the reflector illumination at the edges. To reinforce the credibility of such a result, we shall examine the corresponding AI solution more closely.

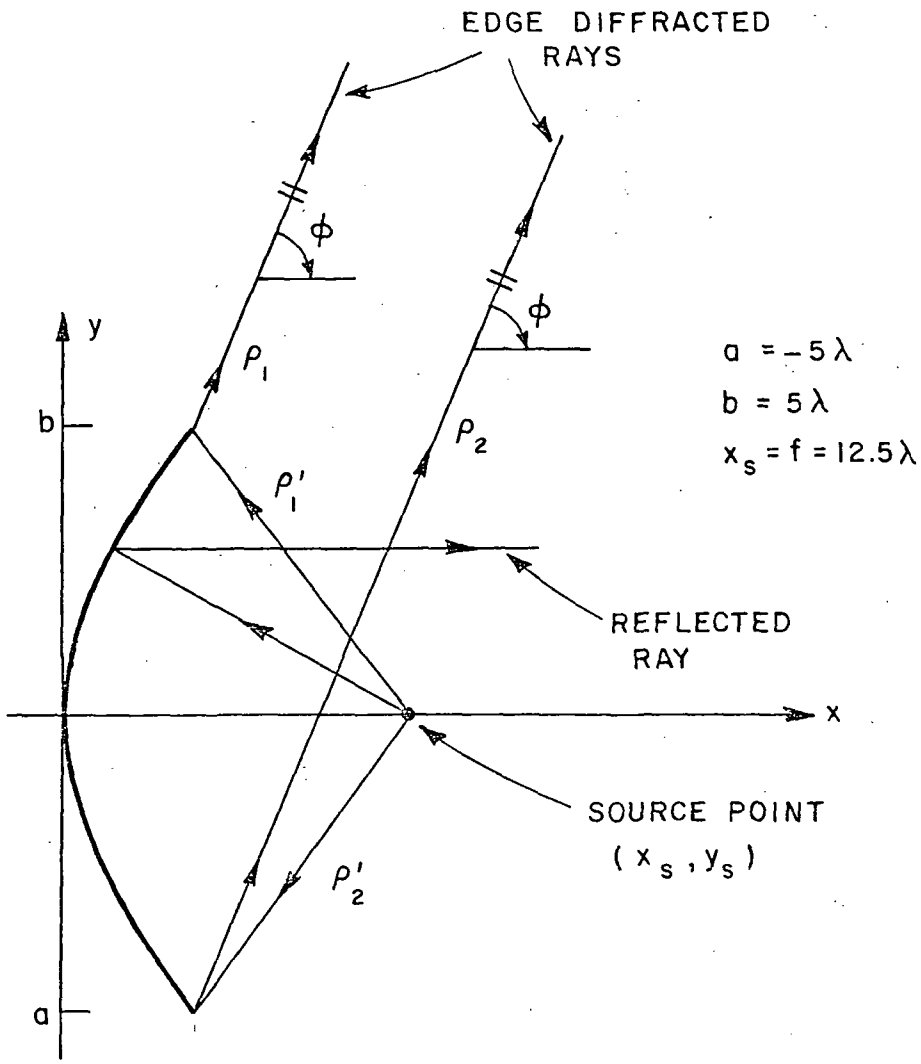

Figure 6.2 Geometry for the far field GTD solution.

Reconsider the far field integral (4.4)

$$H_z(\bar{\rho}) = \frac{e^{-jk\rho}}{\sqrt{\rho}}\sqrt{\frac{jk}{8\pi}}\ 2\cos\phi\ I(\phi)\ , \text{ where}$$

$$I(\phi) \equiv \frac{e^{-jk(\rho_i+\rho_0)}}{\sqrt{f}} \int_{a=-5}^{b=5} e^{jky'\sin\phi}\, dy' \quad .$$

Although this case can be integrated in closed form, this is not the issue we want to pursue. Rather, we wish to show that the result of the integral is only affected by the value of the integrand at the endpoints, or "edges" of the reflector.

The real part of the integrand has been plotted with ϕ a parameter, in Figure 6.3. These results exhibit two very interesting properties. First, we note that $k=2\pi/\lambda$ can always be made large enough so that the integrand oscillates rapidly for $\phi\neq 0$. Choosing k large is the "high frequency assumption" of our solution. Second, we note that for a rapidly oscillating integrand, the positive and negative areas will cancel, until the integration is terminated. This means the only contribution to our solution occurs at the endpoints of integration, i.e., the "edges". Similar reasoning holds for the imaginary part of the integrand, but it is not shown.

From the above discussion, we conclude: given a constant aperture field, the complete far field, high frequency solution for $\phi\neq 0$ is given by the two edge diffracted rays of the GTD solution. This result is extremely important to us, in that we can readily obtain exact, high frequency solutions for the offset and non offset reflectors we have

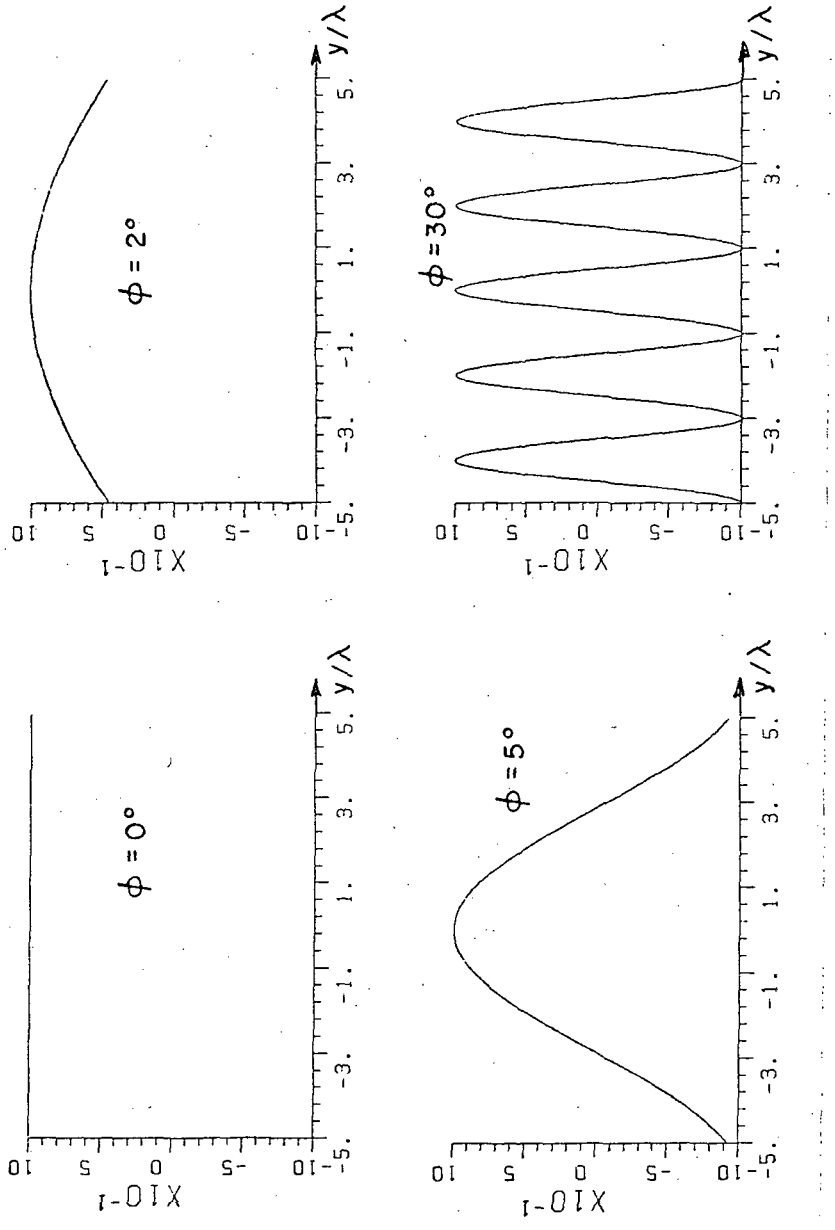

Figure 6.3 Real part of far field integrand, with a uniform aperture field, showing endpoint contributions.

been discussing. The "exact" GTD solutions, found from the two diffracted rays are shown in Figures 5.3 and 5.6 for the non offset and offset cases, respectively.

B. NEAR FIELD GTD AND AI SOLUTIONS WITH A UNIFORM APERTURE FIELD

Let us reconsider the non offset reflector of the previous section with the field point in the near zone. Unlike the far zone case, now the GTD solution consists of three rays. The reflected ray does contribute to the near field solution. In fact, the GTD solution used to calculate the aperture fields of AIE is the near field solution.

The GTD model requires that the reflected and diffracted rays be well defined. One can appreciate that with increasing distance, it becomes increasingly difficult to identify the reflection point on the reflector. This inadequacy of the model for the reflected ray component of the GTD solution is a fundamental limitation of the method.

The next section examines the corresponding near field AI solution. We shall find that not only do the endpoint contributions correspond to edge diffractions, but in addition, the integrand has a point of stationary phase, corresponding to the geometrical optics reflection point.

C. GEOMETRICAL OPTICS AND THE METHOD OF STATIONARY PHASE

With a uniform aperture field, the near field radiation integral (3.4) becomes

$$\bar{H}_z(\bar{\rho}) = \sqrt{\frac{jk}{8\pi}}\, 2\cos\phi\, \frac{e^{-jk\rho_\ell}}{\sqrt{f}}\, I(\bar{\rho}) \qquad (6.1)$$

where

$\rho_\ell \equiv$ path length from the source to the aperture plane (a constant),

$$I(\bar{\rho}) \equiv \rho \int_{-\infty}^{\infty} \frac{e^{-jk\rho_o}}{\rho_o^{3/2}}\, dy' \tag{6.2}$$

and as in Figure 3.2,

$$\rho_o^2 = \rho^2 + y'^2 - 2\rho\, y' \sin\phi \quad .$$

The integral (6.2) is of the form

$$I(\bar{\rho}) = \int_{-\infty}^{\infty} F(y') e^{jkf(y')}\, dy' \tag{6.3}$$

where $F(y)$ is the magnitude, and $f(y)$ is the phase of the integrand. Here, the phase function is

$$-f(y') = \rho_o = \sqrt{\rho^2 + y'^2 - 2\rho\, y' \sin\phi} \quad .$$

It is stationary when $df/dy' = 0$:

$$\frac{df}{dy'} = \frac{y' - \rho \sin\phi}{\sqrt{\rho^2 + y'^2 - 2\rho\, y' \sin\phi}} = 0$$

which occurs at

$$y' = \rho \sin\phi \quad .$$

The point of stationary phase corresponds to the reflection point, as shown in Figure 6.4.

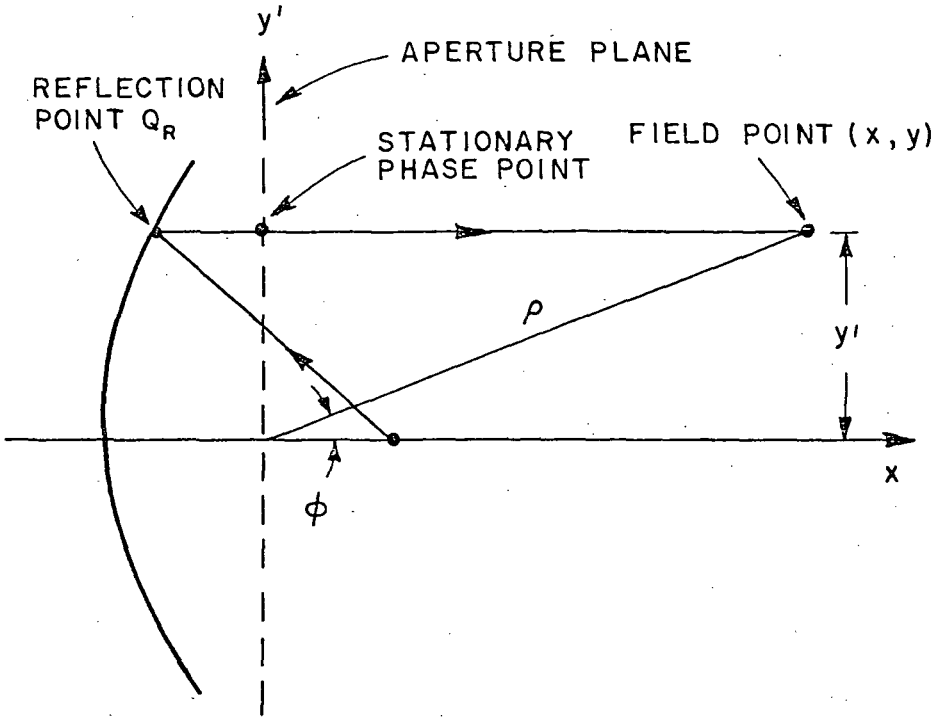

Figure 6.4 Stationary phase point in the aperture plane.

To illustrate the behavior of the integrand, its real part has been plotted for various field points (x,y) in Figure 6.5 and Figure 6.6. From Figure 6.5 we see that with increasing x, the sharpness of the stationary phase point is less pronounced. Figure 6.6 has no stationary phase point.

The near field radiation integral may be evaluated by the method of stationary phase (Appendix D). To apply this method, the phase f(y) must be rapidly varying, where the magnitude F(y) is slowly varying. Applying the prescription of Appendix D to Equation (5.2) we obtain

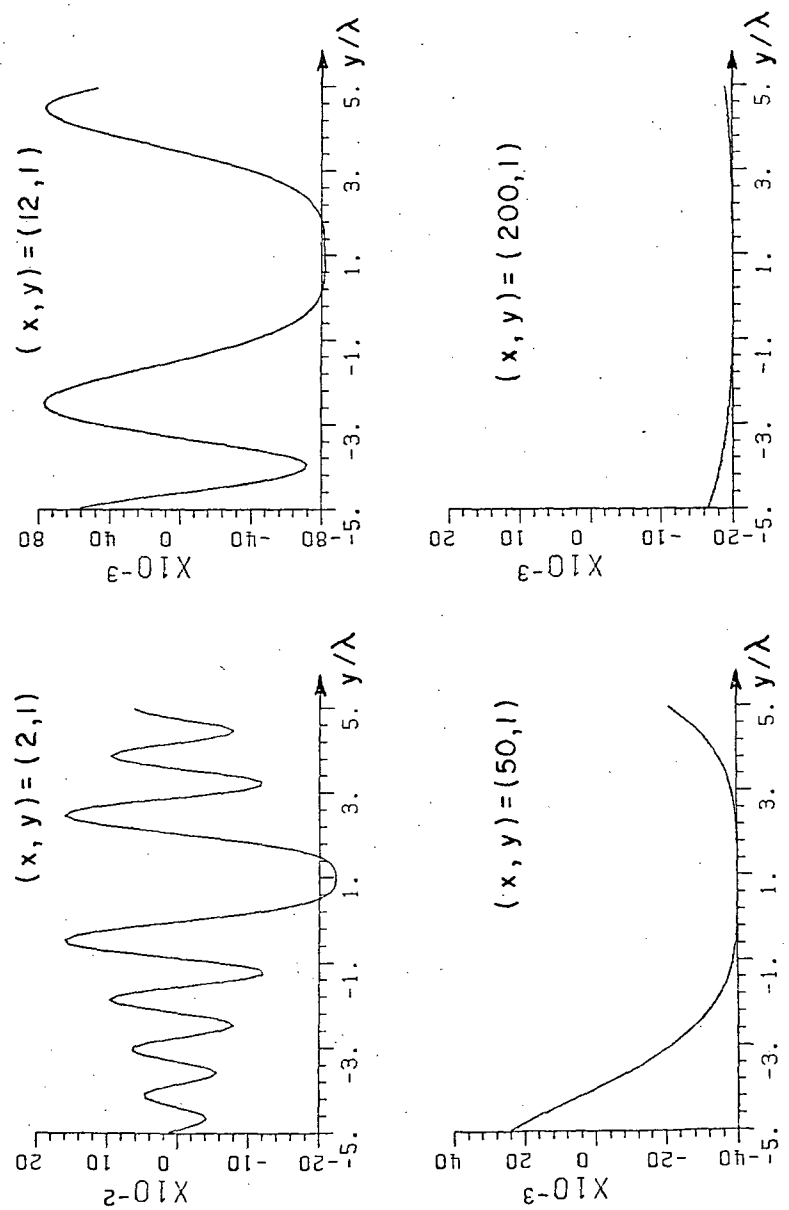

Figure 6.5 Real part of the near field integrand with a uniform aperture field, showing the stationary point and endpoints.

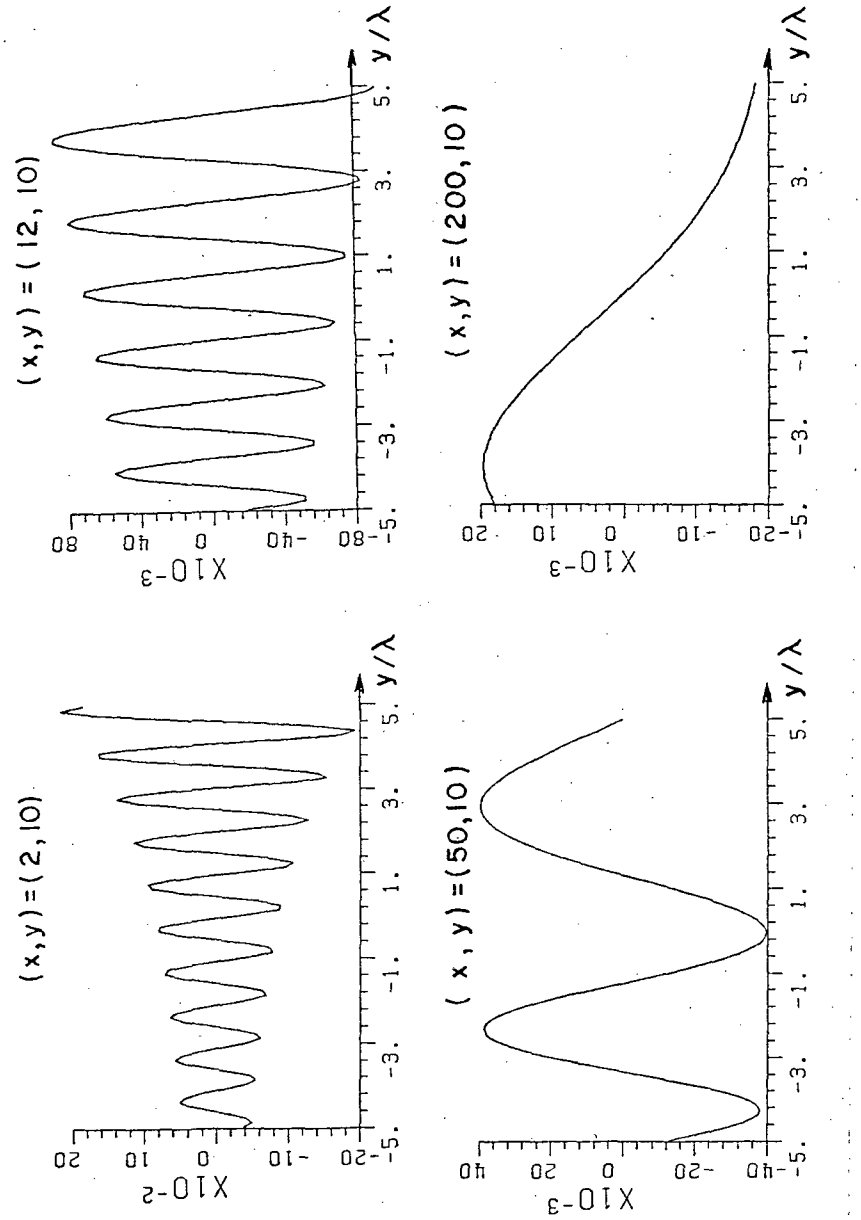

Figure 6.6 Real part of the near field integrand with a uniform aperture field, showing only the endpoint contributions.

$$\bar{I}(\rho) \approx \sqrt{\frac{2\pi}{jk}} \; \frac{e^{-jk\rho\cos\phi}}{\cos\phi} + \text{endpoint contributions} \quad ,$$

so that

$$H_z(\bar{\rho}) = \frac{e^{-jk(\rho_\ell + x)}}{\sqrt{f}} + \text{endpoint contributions} \quad .$$

We recognize that the first term is the same as (4.3), the GO result. Thus we have established the relation between GO and AI via the method of stationary phase.

Near field radiation patterns at a distance of $\rho = 50\lambda$ are shown in Figures 6.7 and 6.8. As expected, we have excellent agreement in the main beam and first few sidelobes.

D. FAR FIELD GTD AND AI SOLUTIONS WITH A NONUNIFORM APERTURE FIELD

The case of a nonuniform aperture field is more troublesome. As in the uniform case, the GTD solution follows from the two edge diffracted rays. Still, the far field GTD pattern only depends on the reflector illumination at the edges. However, we shall find that the extent of the caustic region is much greater than in the far field case with uniform illumination. It will be shown that when the field point is too close to the caustic, the integrand of the AI solution is not suitable for the method of stationary phase.

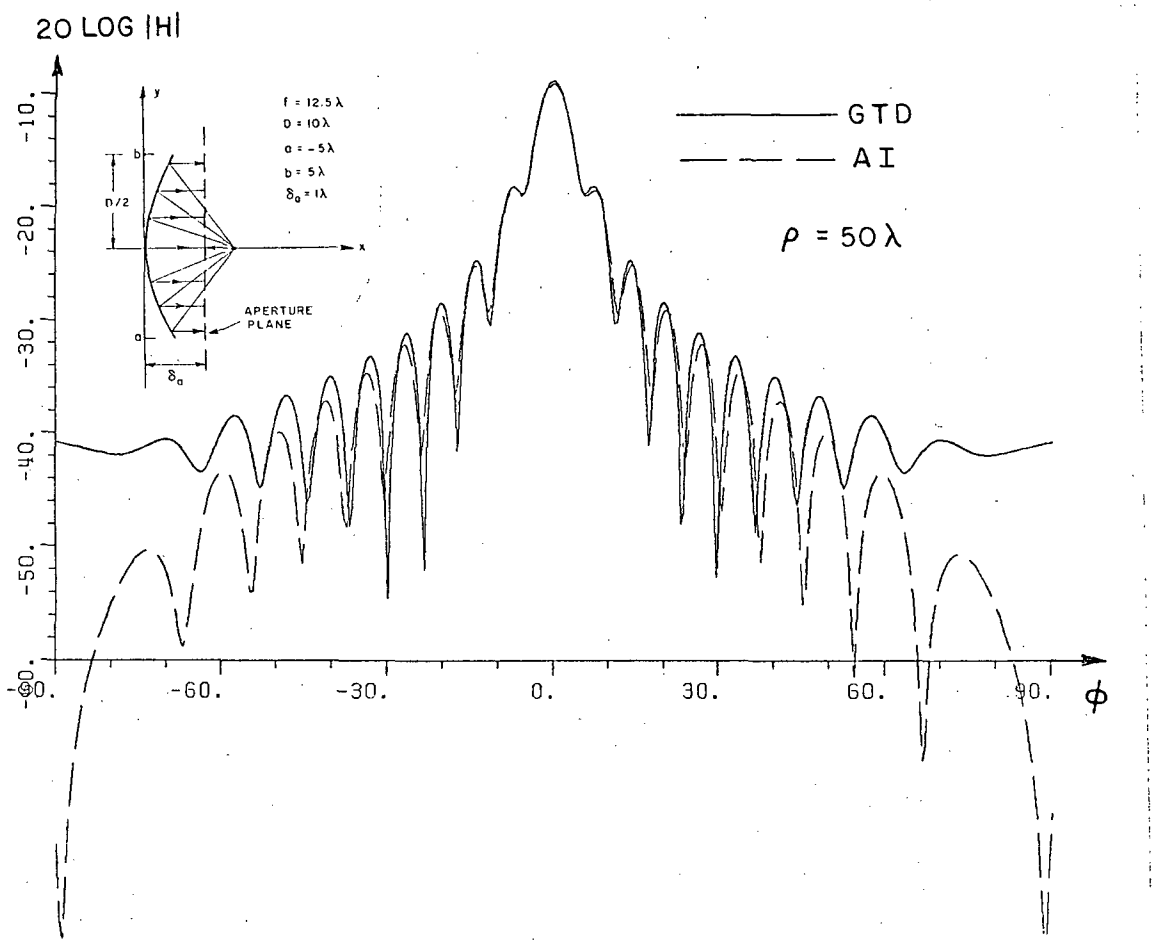

Figure 6.7 Near field radiation pattern at $\rho=50\lambda$, with uniform aperture illumination. AI solution.

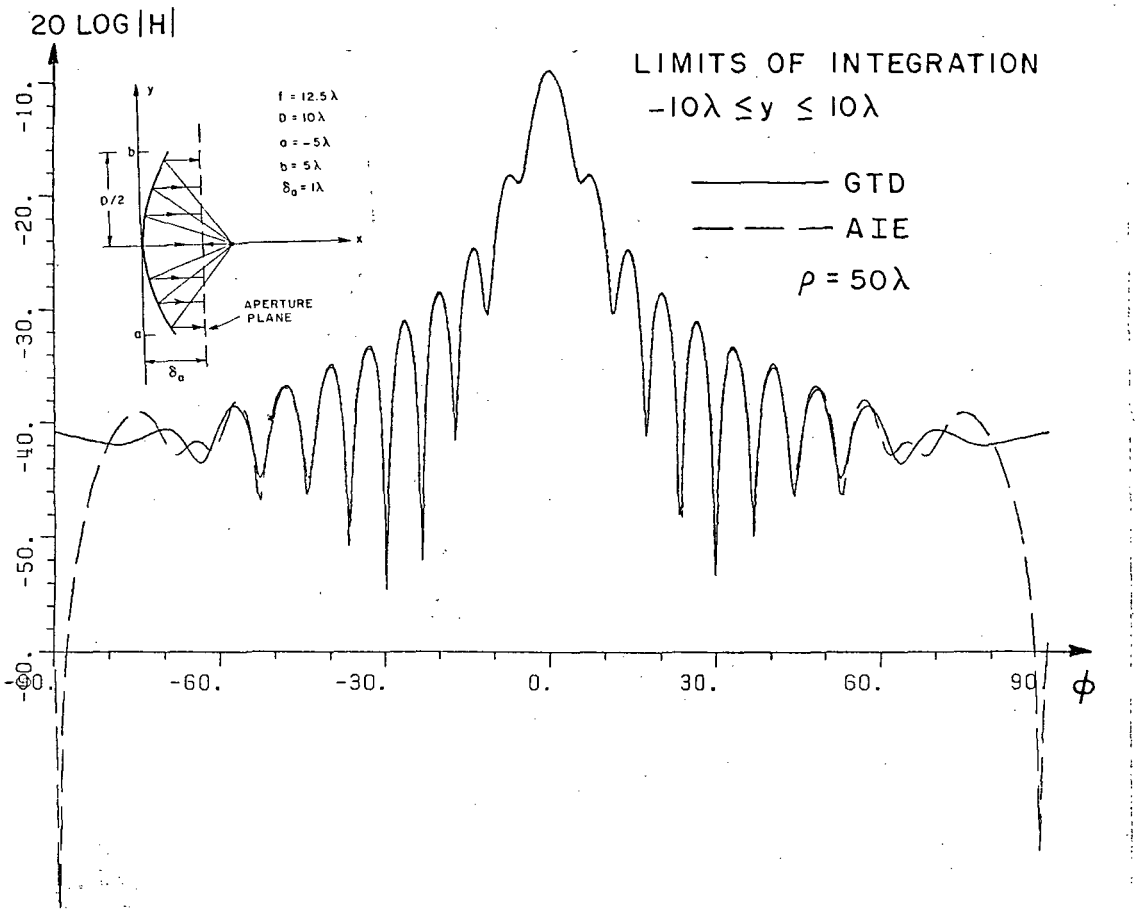

Figure 6.8 Near field radiation pattern at $\rho=50\lambda$, with uniform aperture illumination. AIE solution.

For illustrative purposes, we use a "parabolic squared on a pedestal" aperture illumination, given by

$$F(y) = c + (1-c)\left[1 - \left(\frac{y}{a}\right)^2\right]^2 \qquad \text{with} \tag{6.4}$$

$$a = 5$$

$$c = 0.398 \quad .$$

The edge illumination is 10 dB below the maximum value. The GO and GTD aperture fields along σ_1 of Figure 3.1 for this case are plotted in Figure 6.9. The far field radiation integral (3.5) becomes

$$H_z(\bar{\rho}) = \frac{e^{-jk\rho}}{\sqrt{\rho}}\sqrt{\frac{jk}{8\pi}}\; 2\cos\phi\; I(\bar{\rho}) \qquad \text{where} \tag{6.5}$$

$$I(\bar{\rho}) \equiv \int_{a=-5}^{b=5} H_z(y')\, e^{jky'\sin\phi}\, dy' \quad .$$

As before, we examine the integrand of $I(\bar{\rho})$. The real part has been plotted in Figure 6.10 with ϕ as the parameter. The results are similar to Figure 6.3 except that they have been "modulated" by the amplitude of the aperture field. Far away from the x axis caustic, the integrand oscillates sufficiently rapidly so that positive and negative areas cancel. As before, the only contributions to the integral are from endpoints. However, when the field point is near the x axis, the integrand does not oscillate rapidly. This is where the GTD solution begins to fail. This occurs at about ϕ=30° for our case.

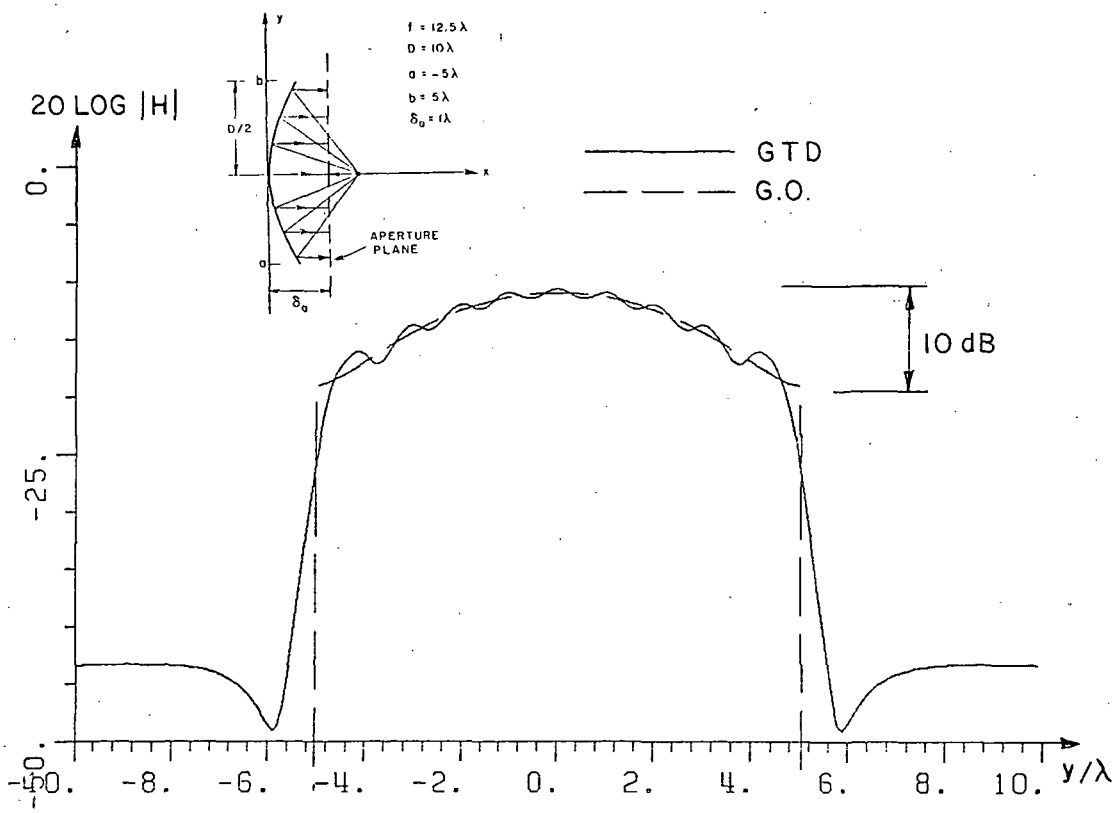

Figure 6.9 Aperture fields for the non offset reflector with magnetic line source illumination and a "parabolic squared on a pedestal" amplitude taper.

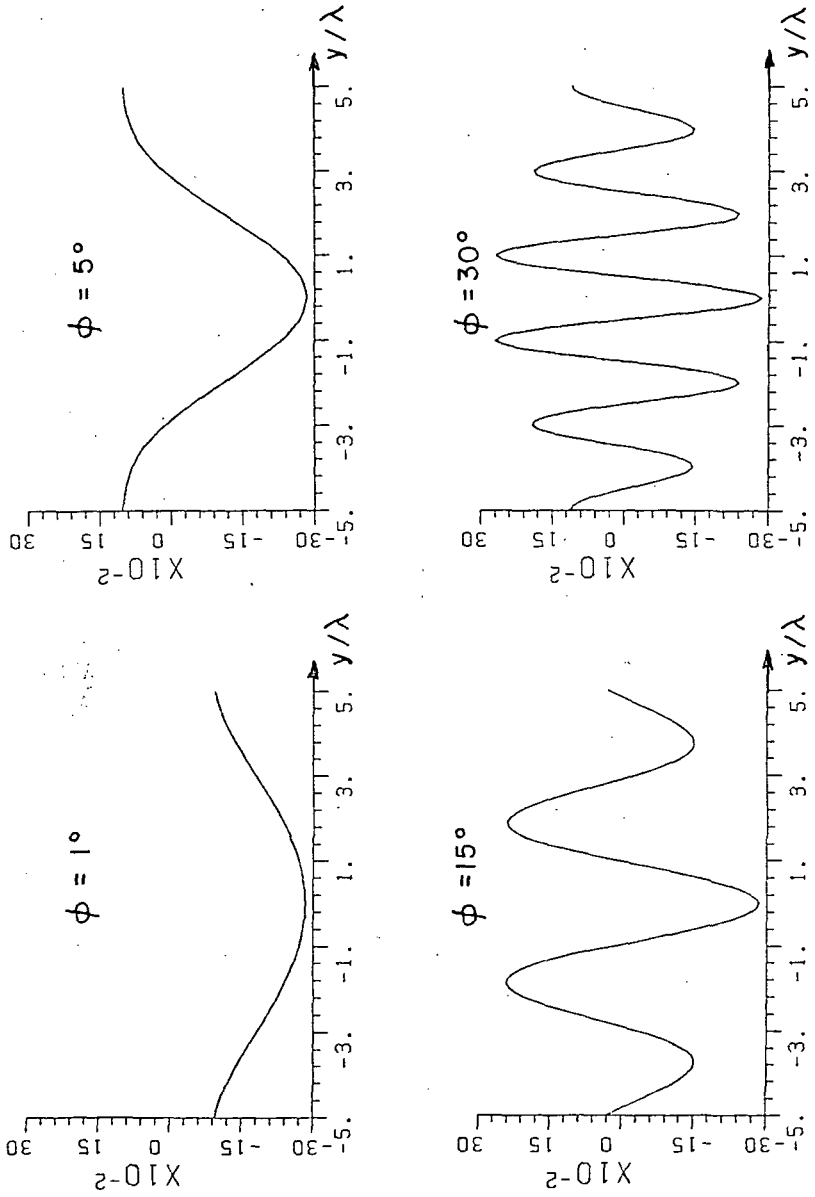

Figure 6.10 Real part of the far field integrand with a nonuniform aperture field, showing endpoint contributions.

From Figure 6.12 we see that the GTD and AIE solutions begin to disagree for $\phi < 30°$. An even more serious problem is that shown in Figure 6.11. The GTD and AI solutions do not overlap at all! It is true that GTD is useful for calculating far out sidelobes and that AI is good for calculating the main beam. In fact, the main beam of the AI and AIE solutions agree quite well. However, it is important to note that AI and GTD solutions do not necessarily have a common region of validity because both have their limitations. The AI has an approximate aperture field with a limited aperture width, whereas GTD has caustic regions within which it is not valid.

E. NEAR FIELD GTD AND AI SOLUTIONS WITH A NONUNIFORM APERTURE FIELD

We have already used the near field GTD solution to calculate the extended aperture fields of the previous section. The field point in such a case is deep in the near field, so that the solution is generally well behaved. Rather, what we need to investigate here is: How far away from the antenna, along the reflector axis, does the GTD solution begin to fail? Or equivalently, what is the extent of the caustic region?

Our discussion is again based on the behavior of the AI solution's integrand. We have

$$H_z(\rho) = \sqrt{\frac{jk}{8\pi}}\; 2\cos\phi\; I(x,y) \quad , \text{ where}$$

$$I(x,y) \equiv \int_{a=-5}^{b=5} \frac{\rho}{\rho_o}\; H_z(y')\; \frac{e^{-jk\rho_o}}{\sqrt{\rho_o}}\; dy' \tag{6.6}$$

which follows from (3.4).

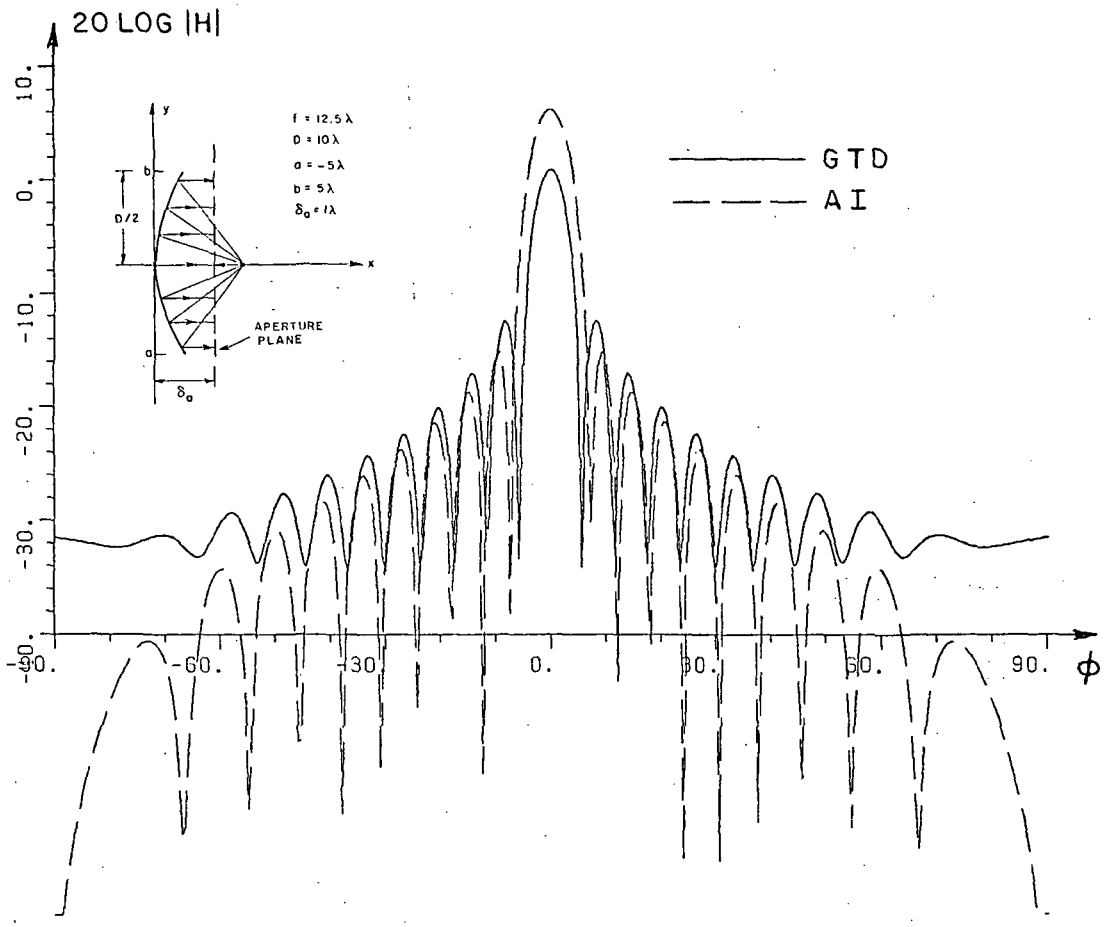

Figure 6.11 Far field radiation pattern with nonuniform aperture illumination. AI solution.

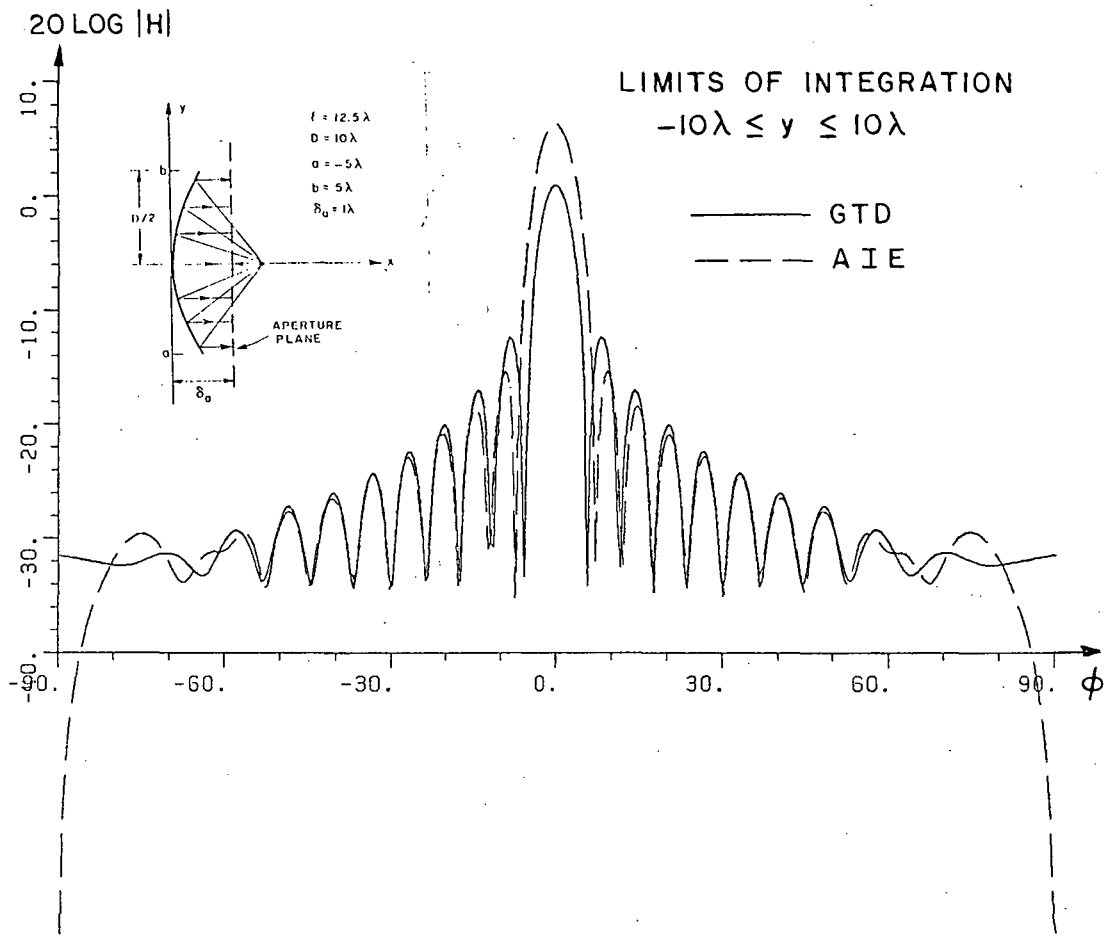

Figure 6.12 Far field radiation pattern with nonuniform aperture illumination. AIE solution.

The integrand has been plotted for several field points in Figures 6.13 and 6.14.

From Figure 6.13 we see that deep in the near field, when $(x,y) = (2,1)$, the integrand oscillates sufficiently rapidly so that the method of stationary phase can be applied. However, at $(x,y) = (12,1)$ the "modulation" due to the aperture field taper is no longer slowly varying with respect to the oscillations of the integrand. We see that with increasing x, positive and negative contributions to the integral will not cancel. Because these cancellations are no longer occurring, we no longer have well defined stationary point and endpoint contributions. We are unable to model the reflector in terms of these three contributions. Consequently, the GTD solution begins to fail for large ρ, near the reflector axis. This should come as no surprise, because one of the basic postulates of GTD ils that it fails at and near caustics. The x axis at infinity is a caustic of reflected rays for a focussed parabola.

Figures 6.15 through 6.17 compare AI with GTD. Figures 6.18 and 6.20 compare AIE with GTD. The point of interest here is not that AIE works better than AI, but that GTD fails when the method of stationary phase fails, i.e., at large ρ, near the reflector axis. From these figures, we see that this is a problem, even in the Fresnel zone, at $\rho=50\lambda$.

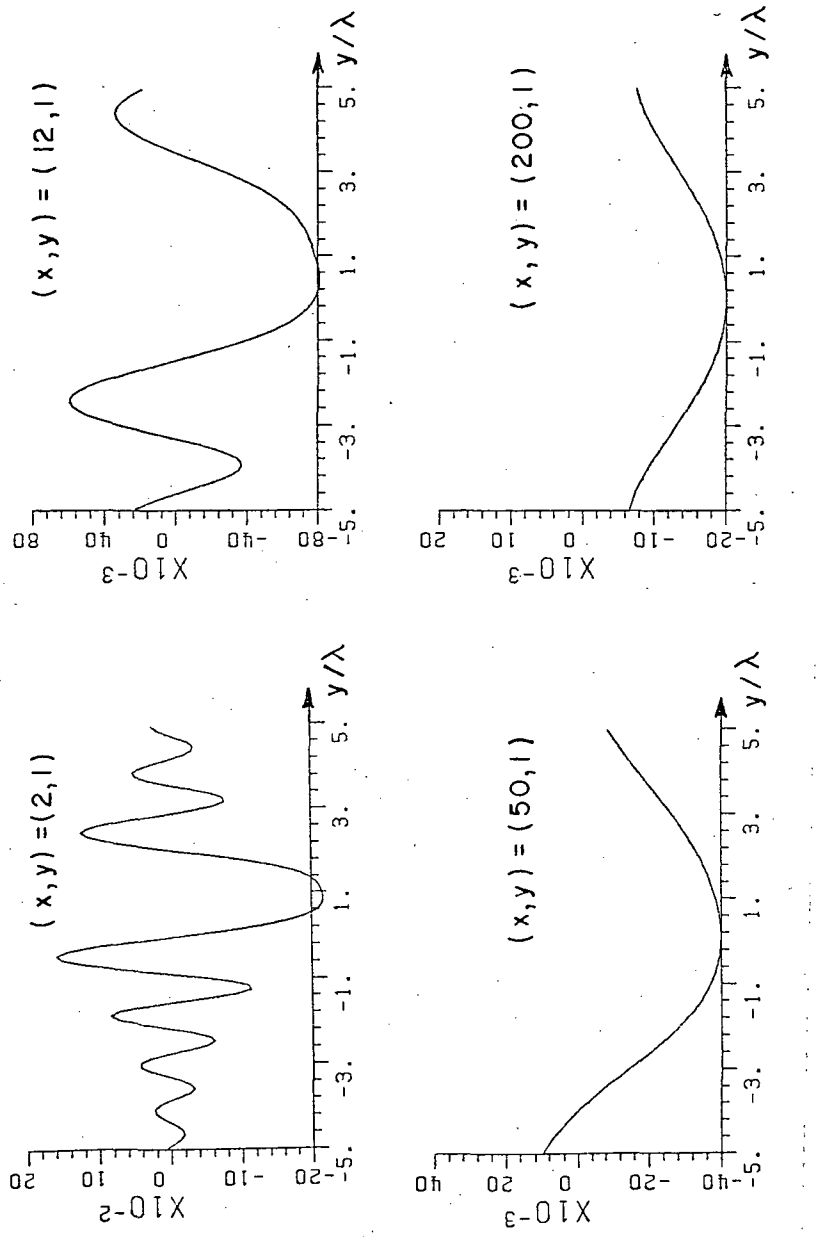

Figure 6.13 Real part of the near field integrand showing the effect of an amplitude taper. Two endpoints and a stationary point are present.

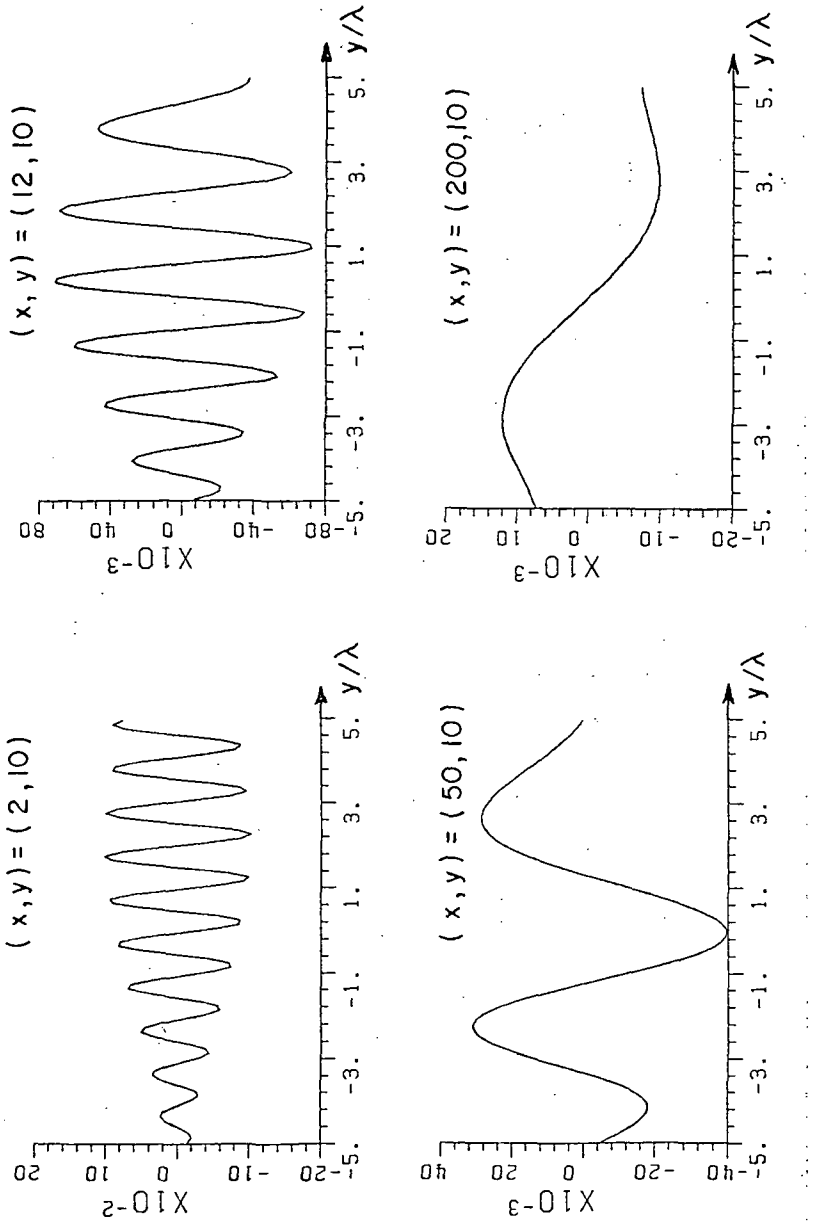

Figure 6.14 Real part of the near field integrand showing the effect of an amplitude taper. Only endpoint contributions are present.

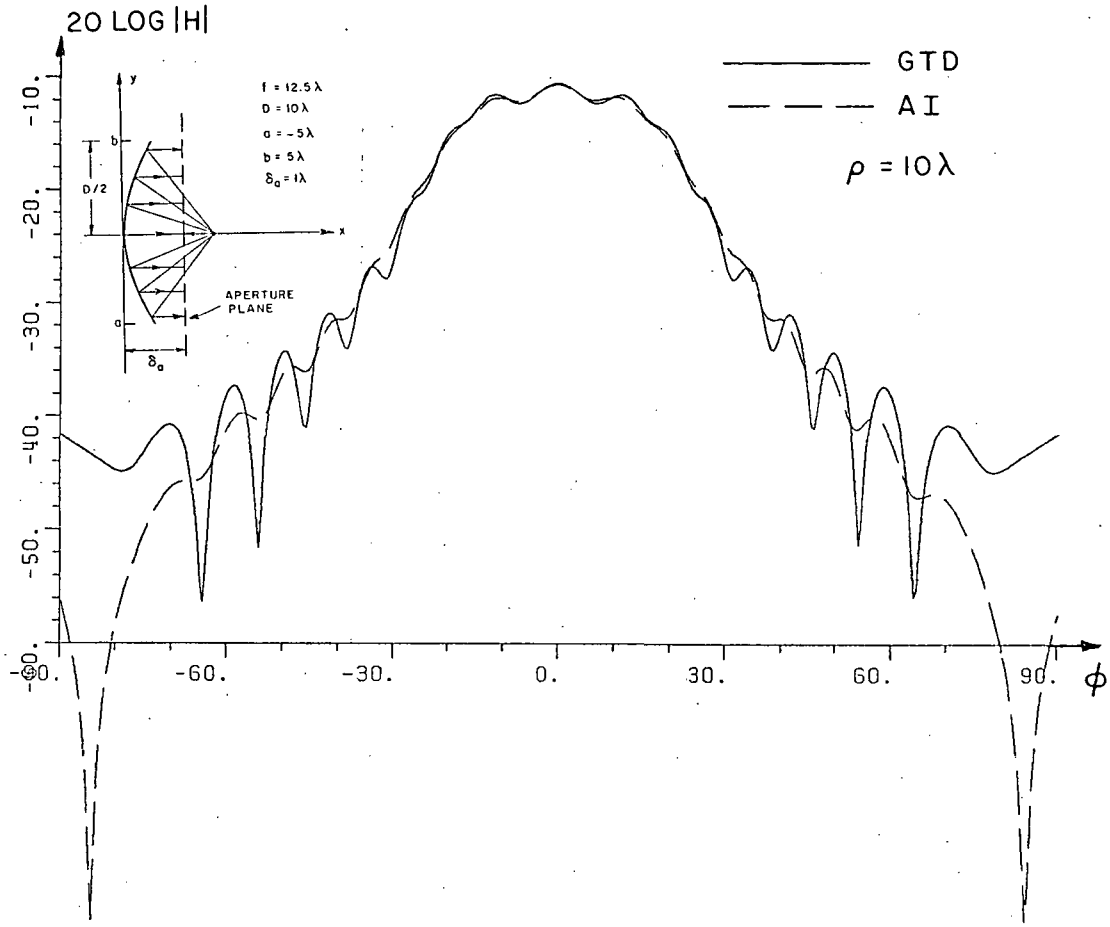

Figure 6.15 Near field radiation pattern at $\rho=10\lambda$, with nonuniform aperture illumination. AI solution.

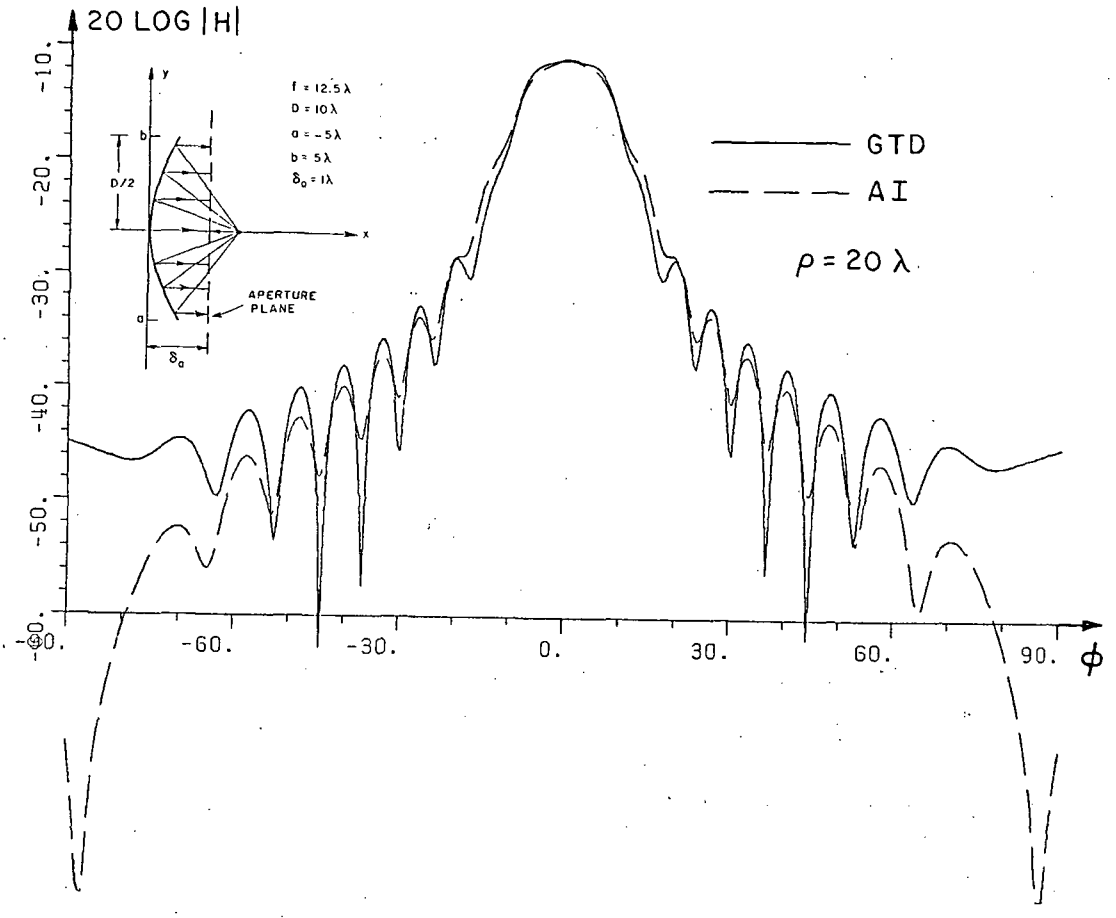

Figure 6.16 Near field radiation pattern at $\rho=20\lambda$ with nonuniform aperture illumination. AI solution.

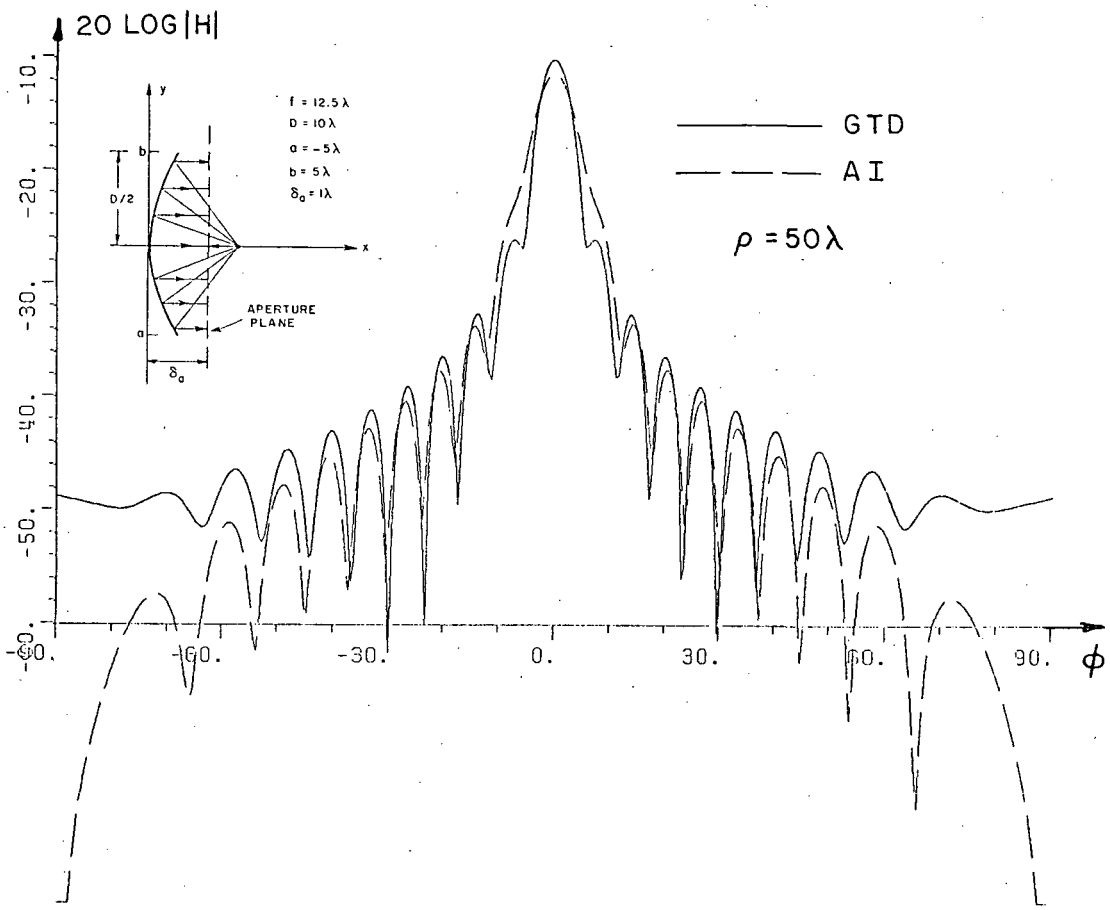

Figure 6.17 Near field radiation pattern at $\rho=50\lambda$ with nonuniform aperture illumination. AI solution.

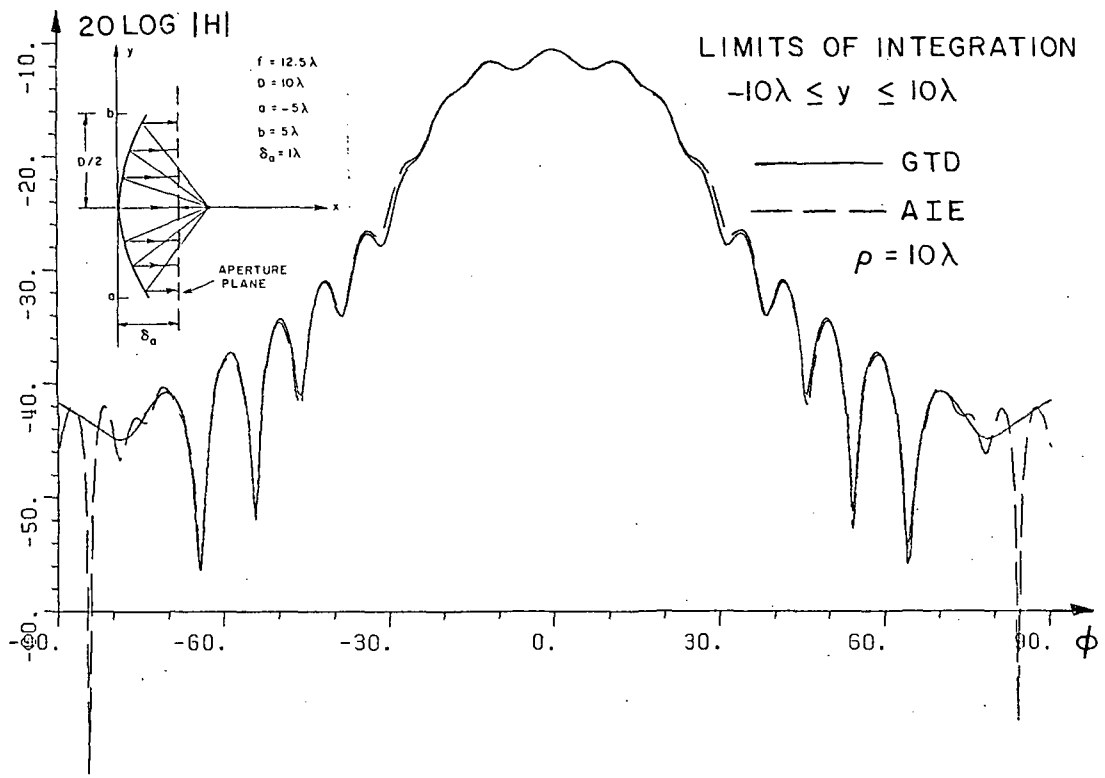

Figure 6.18 Near field radiation pattern at $\rho=10\lambda$ with nonuniform illumination. AIE solution.

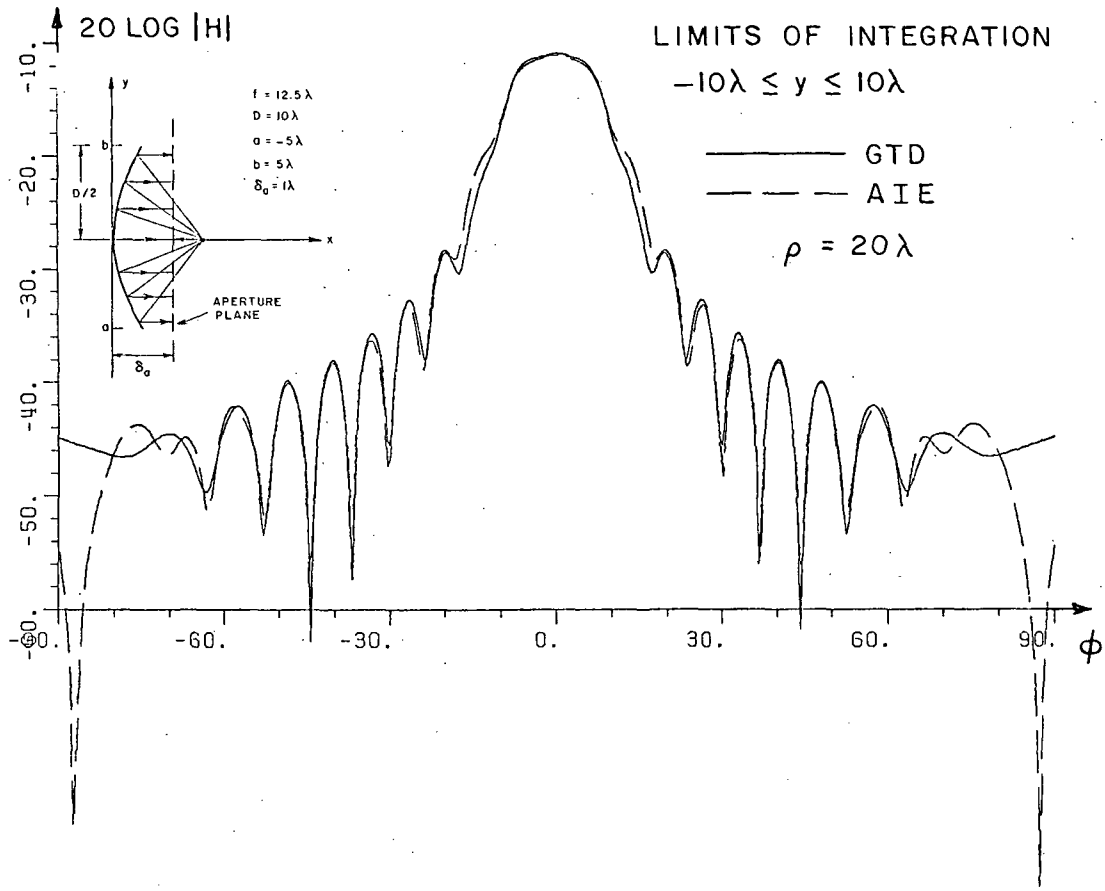

Figure 6.19 Near field radiation pattern at $\rho=20\lambda$ with nonuniform aperture illumination. AIE solution.

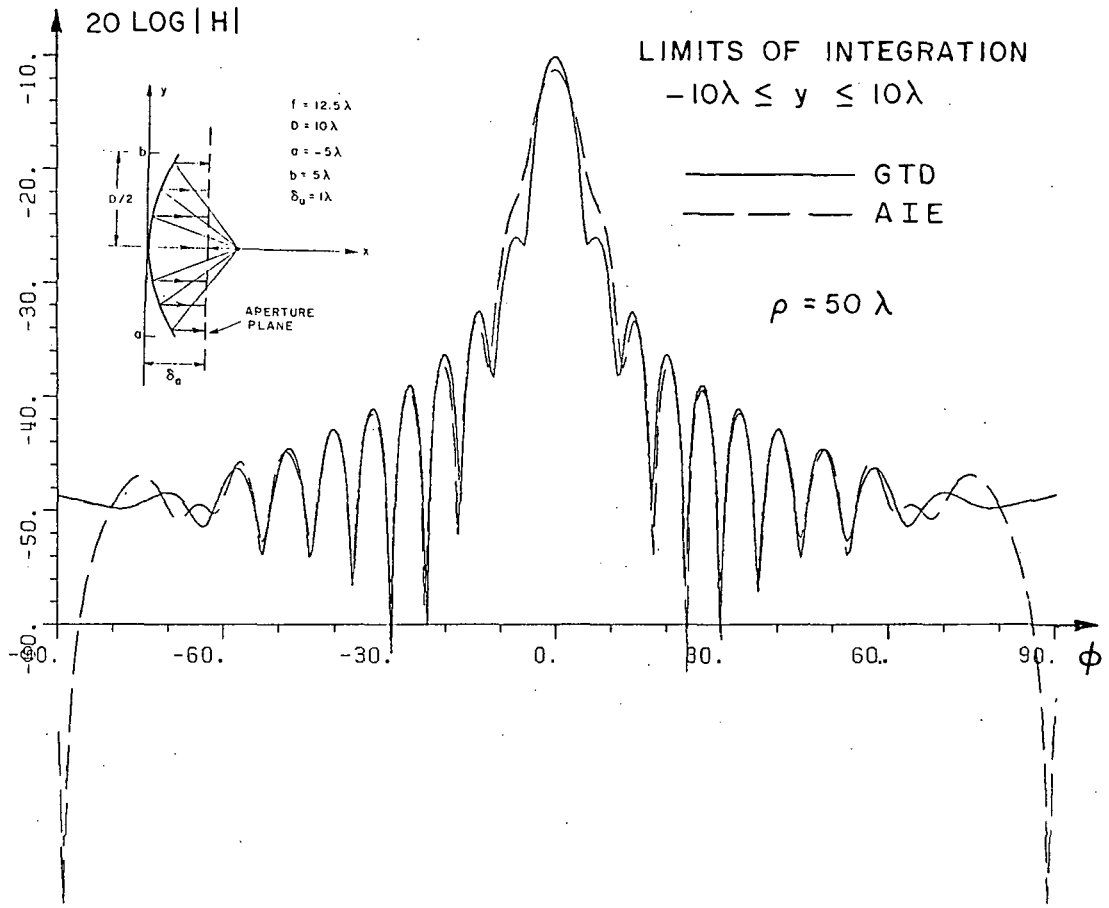

Figure 6.20 Near field radiation pattern at $\rho=50\lambda$ with nonuniform aperture illumination. AIE solution.

CHAPTER VII

CHOOSING THE LIMITS OF INTEGRATION FOR AIE

Since it becomes impractical to carry out an aperture integration over a very large aperture plane, choosing the limits of integration deserves more investigation.

The most serious errors in using aperture fields calculated from GO occur when: (1) the illumination of the reflector edge is strong, and when (2) the reflector edge is not close to the aperture plane.

As a case study, we examine the offset reflector of Figure 4.2 with uniform illumination. The aperture field for this case is shown in Figure 5.5, and is plotted again for a greater range of y, in Figure 7.1 The results of varying the limits of integration are shown in Figure 7.2 through 7.4. In all three cases, the aperture field used is calculated from GTD.

By extending the aperture 3λ on the lower edge and 2λ on the upper edge, a substantial improvement in the far field radiation pattern occurs. This can be seen by comparing Figure 7.3 and Figure 7.2. On the other hand, we see from Figure 7.4 that little more is gained by extending the aperture plane by 30λ on both sides of the reflector.

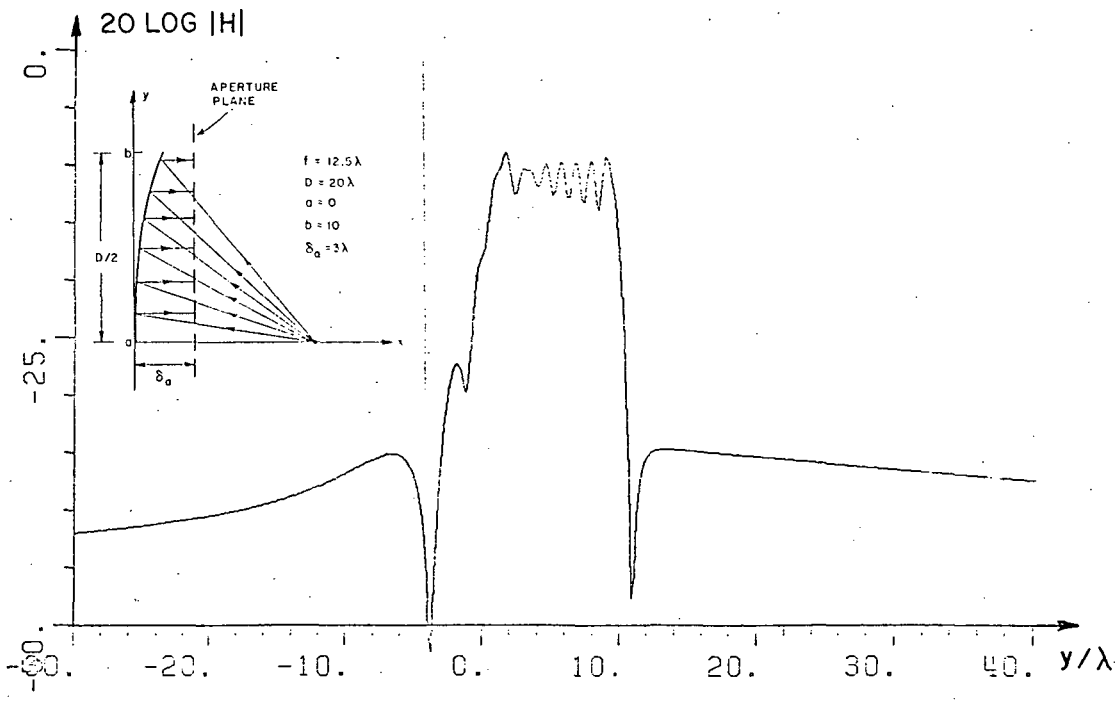

Figure 7.1 Aperture fields for the offset reflector with magnetic line source illumination.

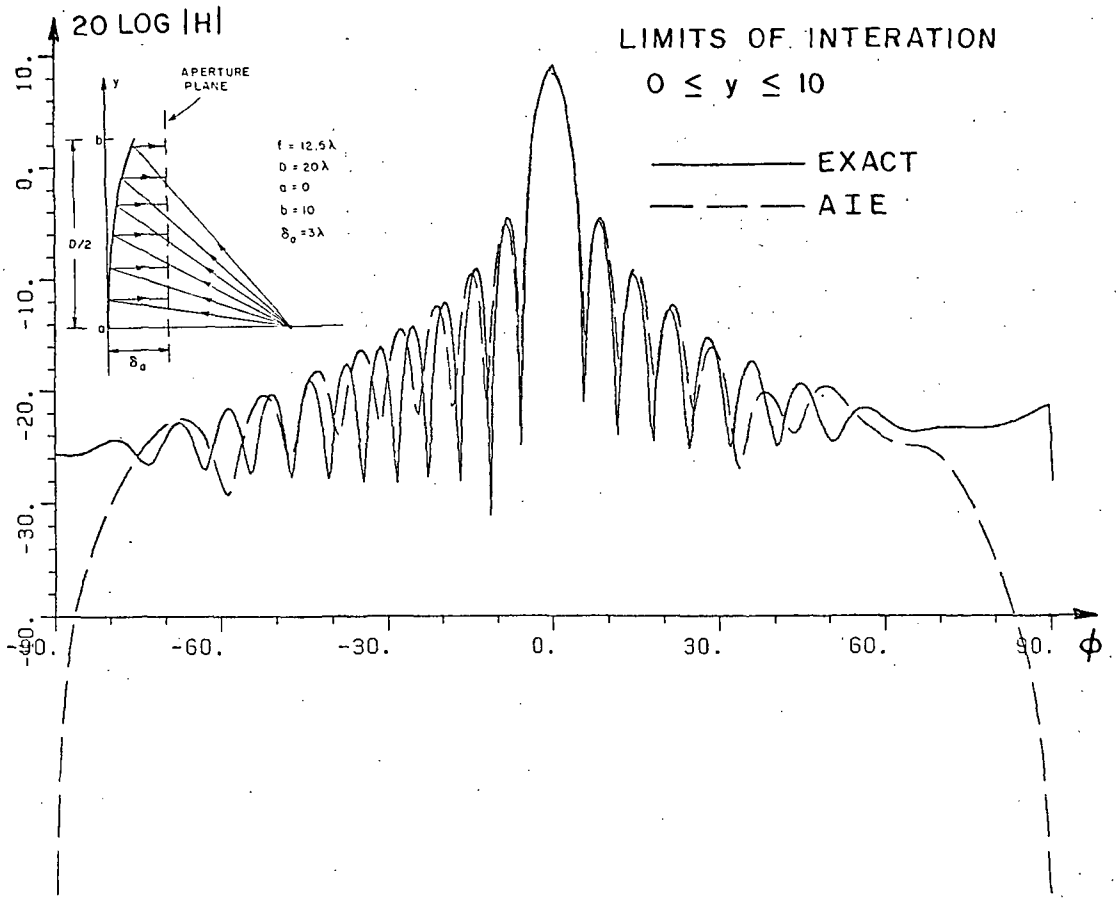

Figure 7.2 Far field radiation pattern for the offset reflector.

Limits of integration are $0 \leq y \leq 10\lambda$.

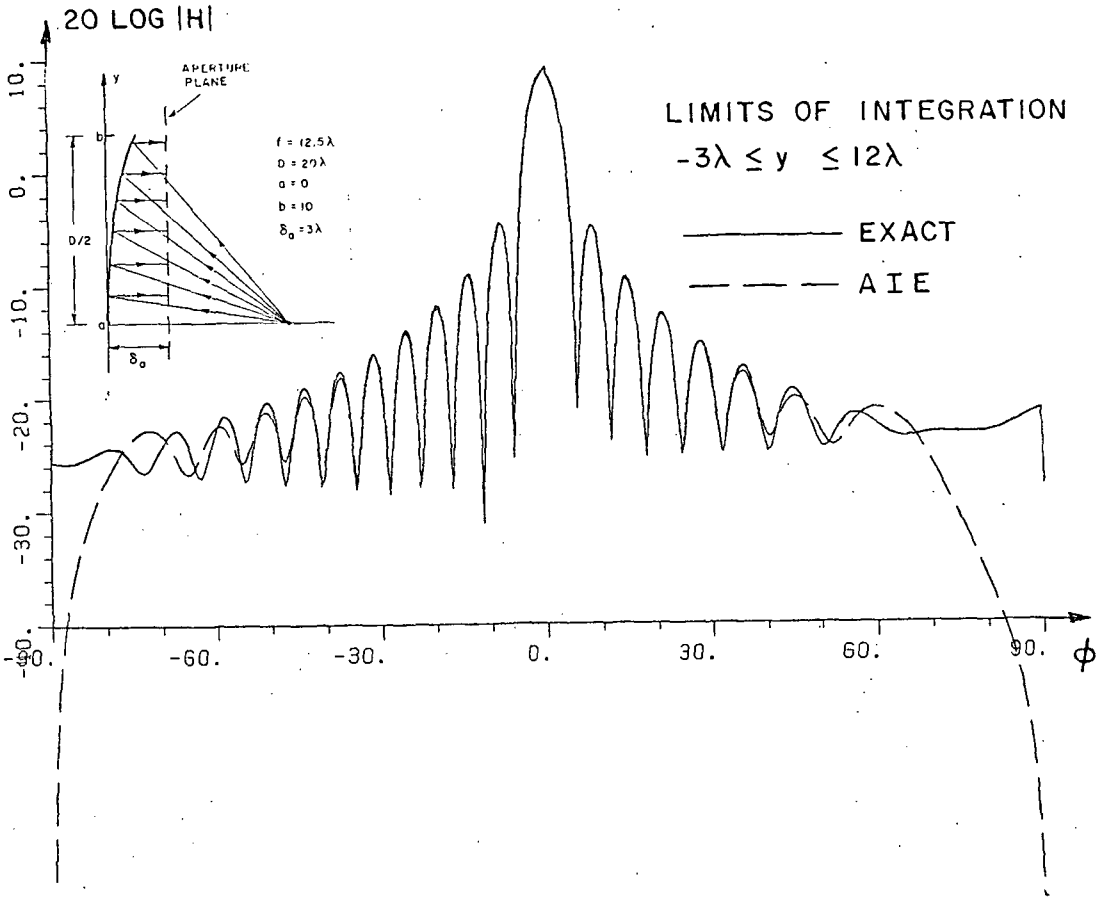

Figure 7.3 Far field radiation pattern for the offset reflector.

Limits of integration are $-3\lambda \leq y \leq 12\lambda$.

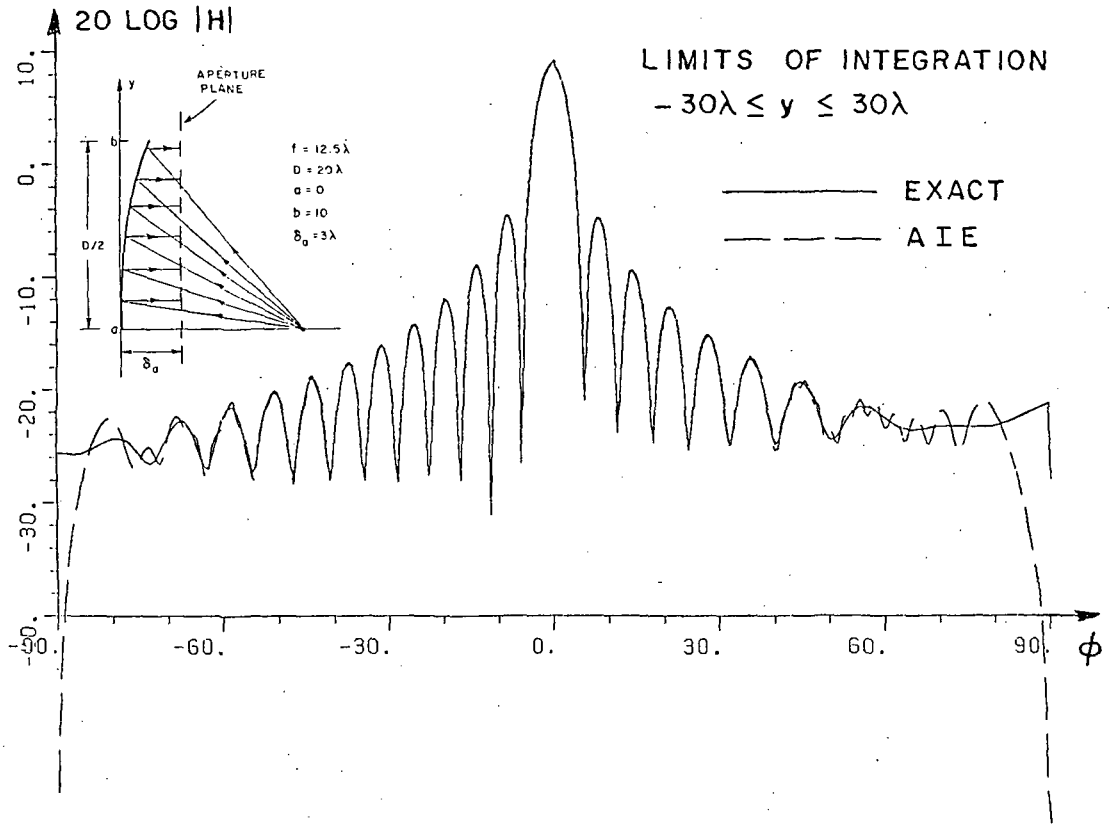

Figure 7.4 Far field radiation pattern for the offset reflector. Limits of integration are $-30\lambda \leq y \leq 30\lambda$.

The aperture field of Figure 7.1 is rapidly varying, near the reflection boundaries at y=0 and y=10. Near these regions, the transition function F in the diffraction coefficient D_h (see Appendix C) compensates for discontinuities in the reflected field. Of the four terms in D_h, the one which compensates for a discontinuity in reflection from the "0" face of the reflector is the fourth term of Equation (C.3):

$$\frac{-e^{-j\pi/4}}{2n\sqrt{2\pi k}} \cot\left(\frac{\pi-(\psi+\psi')}{2n}\right) F(kL^{ro}a^{-}(\psi+\psi')) \ . \qquad (7.1)$$

The region where the aperture field is rapidly varying is known as a "transition region" [2], and the argument of F is less than 2π in that region.

The values of $kL^{ro}a$ for the upper and lower edges are in Table 7.1 as a function of y. For the upper edge, $kL^{ro}a > 2\pi$ when $y \geq 12$. For the lower edge, $kL^{ro}a > 2\pi$ when $y \leq -3$. This suggests little is gained by integrating the aperture field beyond the extent of its transition regions. The convergence of the AIE solution to the correct result is extremely slow past the fifth sidelobe or so.

TABLE 7.1

kLa PARAMETERS FOR THE APERTURE FIELD

APERTURE POINT	UPPER EDGE	LOWER EDGE
y/λ	kL^{ro}_a	kL^{ro}_a
-5.0	88.174	17.787
-4.0	81.906	12.566
-3.0	75.640	7.808
-2.0	69.376	3.805
-1.0	63.117	1.020
-0.0	56.862	0.000
1.0	50.613	1.020
2.0	44.373	3.805
3.0	38.146	7.808
4.0	31.936	12.566
5.0	25.755	17.787
6.0	19.623	23.299
7.0	13.586	29.002
8.0	7.766	34.834
9.0	2.603	40.758
10.0	0.000	46.749
11.0	2.603	52.790
12.0	7.766	58.869
13.0	13.586	64.979
14.0	19.623	71.112
15.0	25.755	77.265
16.0	31.936	83.433

CHAPTER VIII

ADDITIONAL RESULTS

In this chapter, a two dimensional counterpart of the Chu-Turrin offset reflector is examined. This case has the following parameters:

aperture width $D/2 = 18.8\lambda$

focal distance $f = 9.4\lambda$

and is shown in Figure 8.1.

Unlike our previous investigations, an electric line source feed is used, with a parabolic on a pedestal aperture field given by

$$F(y) = \{ C + (1-C) \left[1 - \left(\frac{y-a}{a}\right)^2\right] \} \sqrt{f}$$

where

$a = 9.40$

$C = 0.211$

The maximum value occurs at the center of the aperture, and the edge illumination is down by 13.5 dB. The $1/\sqrt{f}$ amplitude taper of the reflector has been neglected in this analysis.

The aperture plane is positioned at $\delta_{AP} = 10\lambda$. This is 0.6λ away from the reflector edge. The GO and GTD aperture fields have been plotted in Figure 8.2. Its GTD transition regions extend to about -5λ at the lower edge, and 21λ at the upper edge. Resulting AI and AIE solutions for the far field radiation patterns are shown in Figures 8.3 and 8.4.

We see that by integrating over the extent of the aperture field transition regions, the AIE and GTD solutions will overlap at $\phi = -15°$ and $\phi \approx 18°$. Inside this region, the GTD solution is too low because it is failing near a caustic. Outside this region, the AIE solution is too low because the integration is not carried out over an infinite aperture plane.

Figure 8.4 represents about the best result that can be expected from an AIE solution. Figure 8.5 shows the AIE solution when the aperture plane has been extended by 20λ on either side of the reflector. We see that very little is gained from integrating beyond the aperture field transition regions. In fact, the AIE result converges to the GTD result extremely slowly, past the fourth or fifth sidelobe.

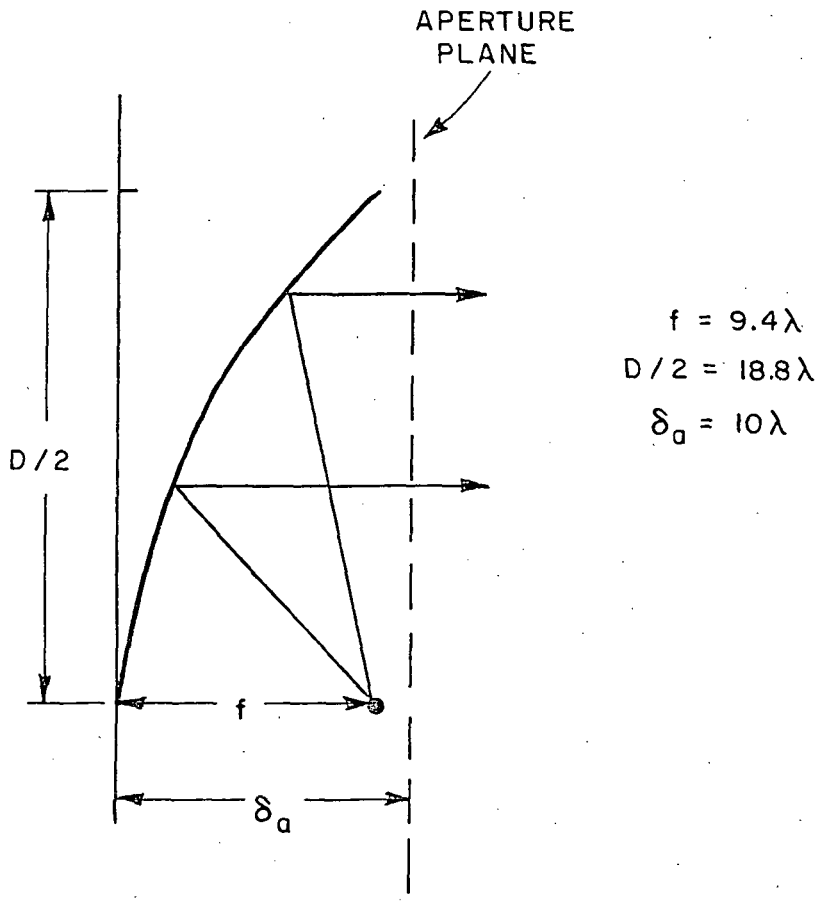

Figure 8.1 Two dimensional model of the Chu-Turrin offset reflector.

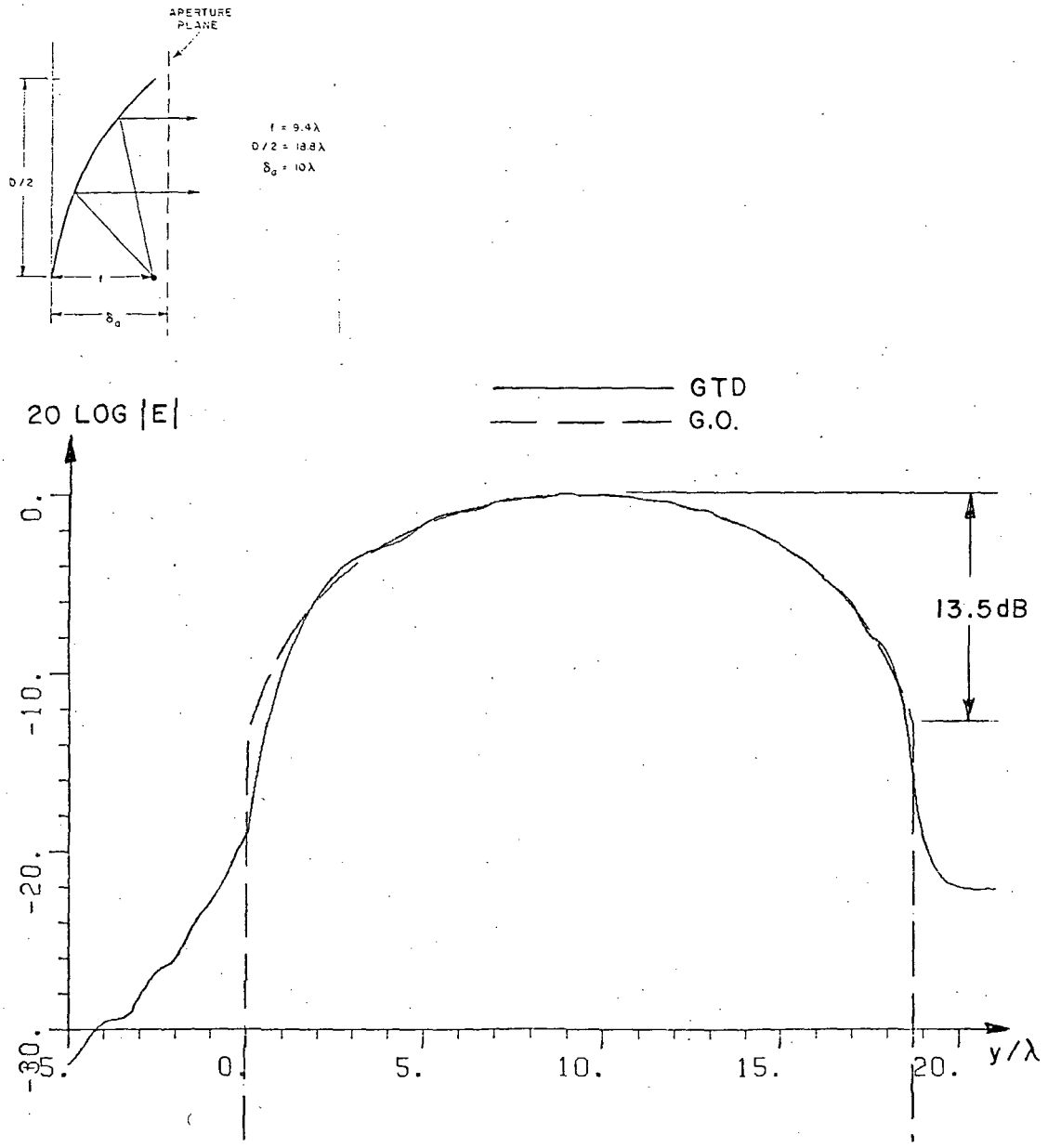

Figure 8.2 Aperture field for the reflector, with electric line source illumination and a "parabolic on a pedestal" amplitude taper. f = 9.4λ, and D/2 = 18.8λ.

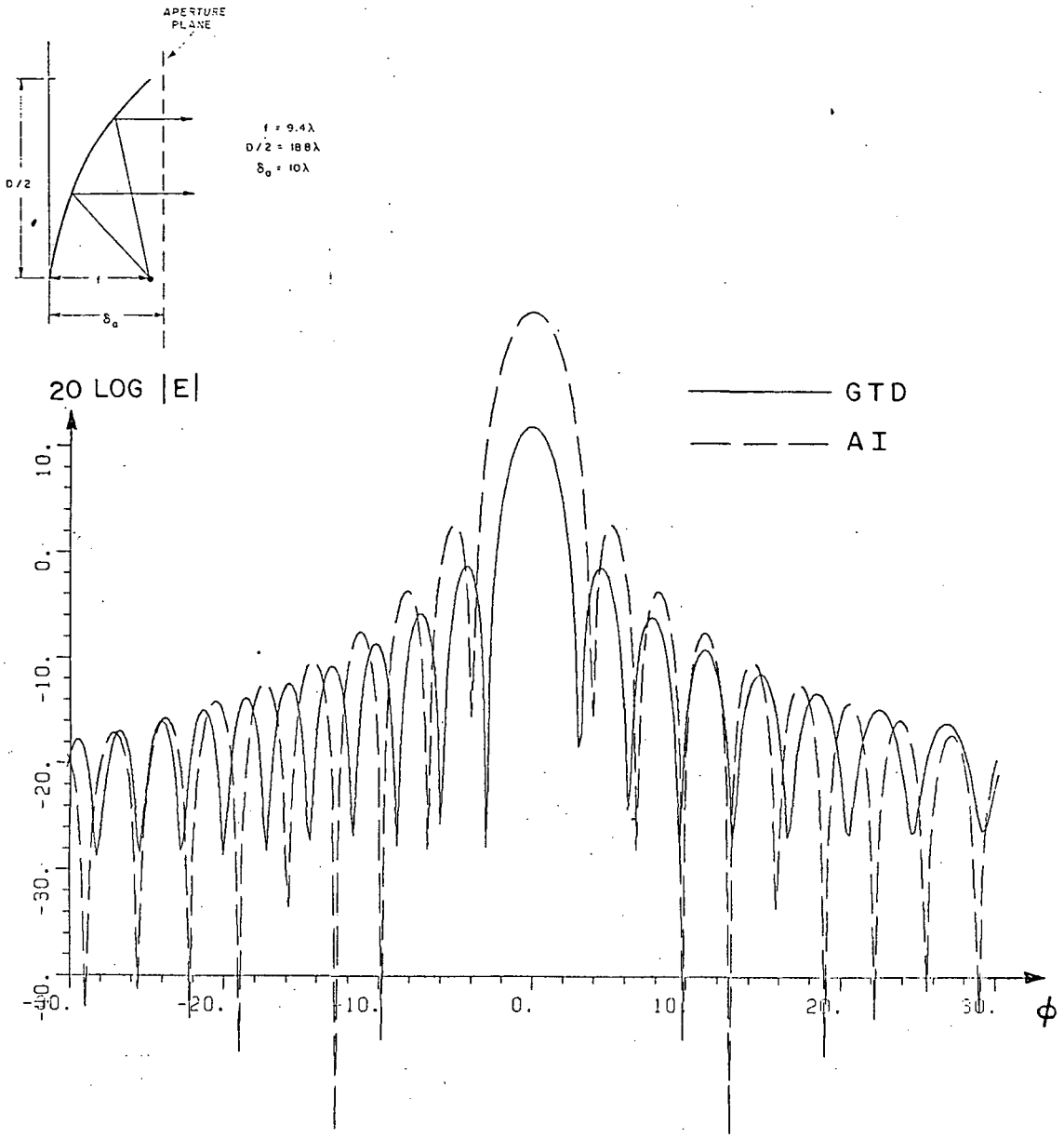

Figure 8.3 Far field radiation pattern with nonuniform perture illumination. AI solution.

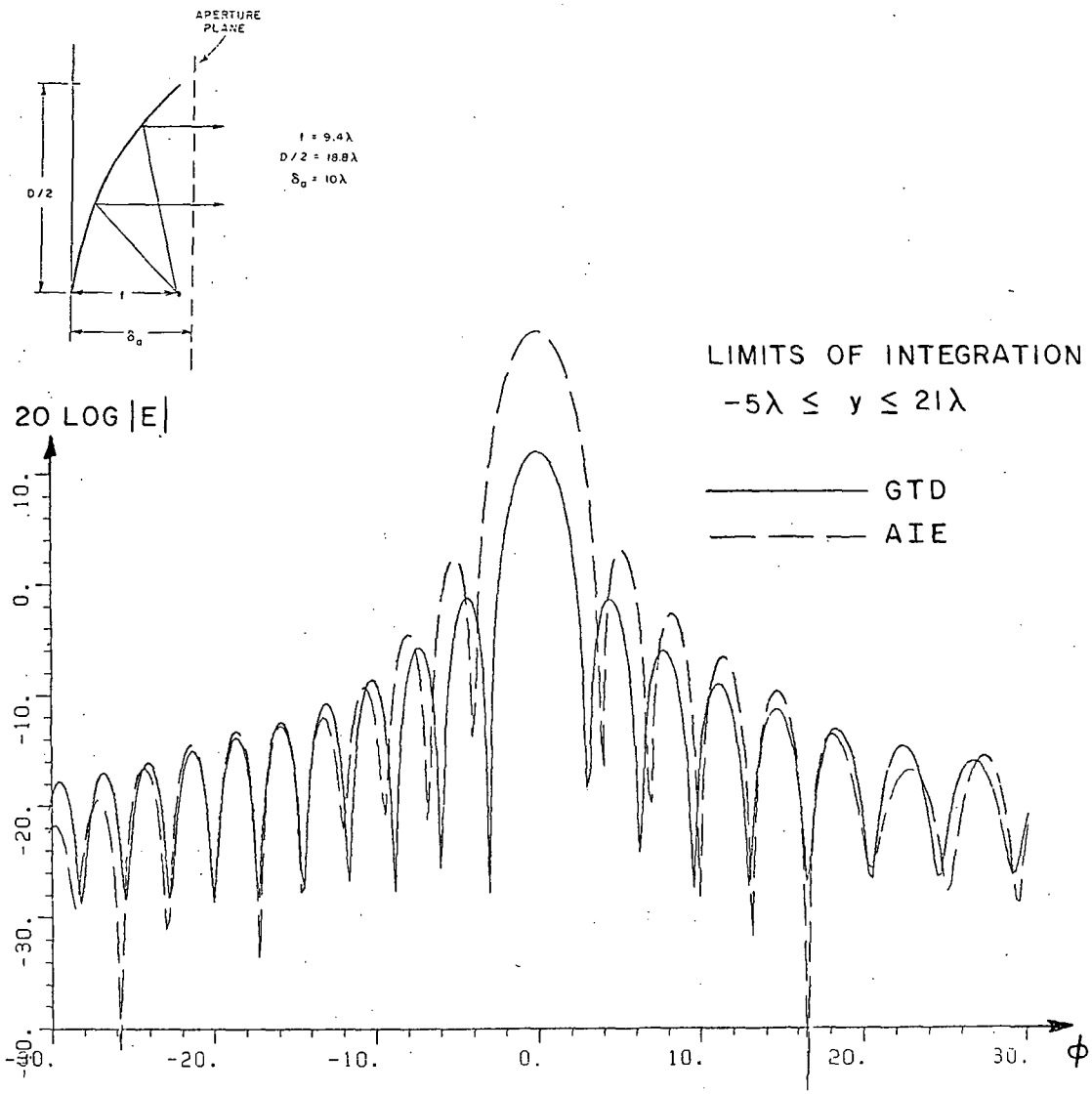

Figure 8.4 Far field radiation pattern with nonuniform aperture illumination. AIE solution.

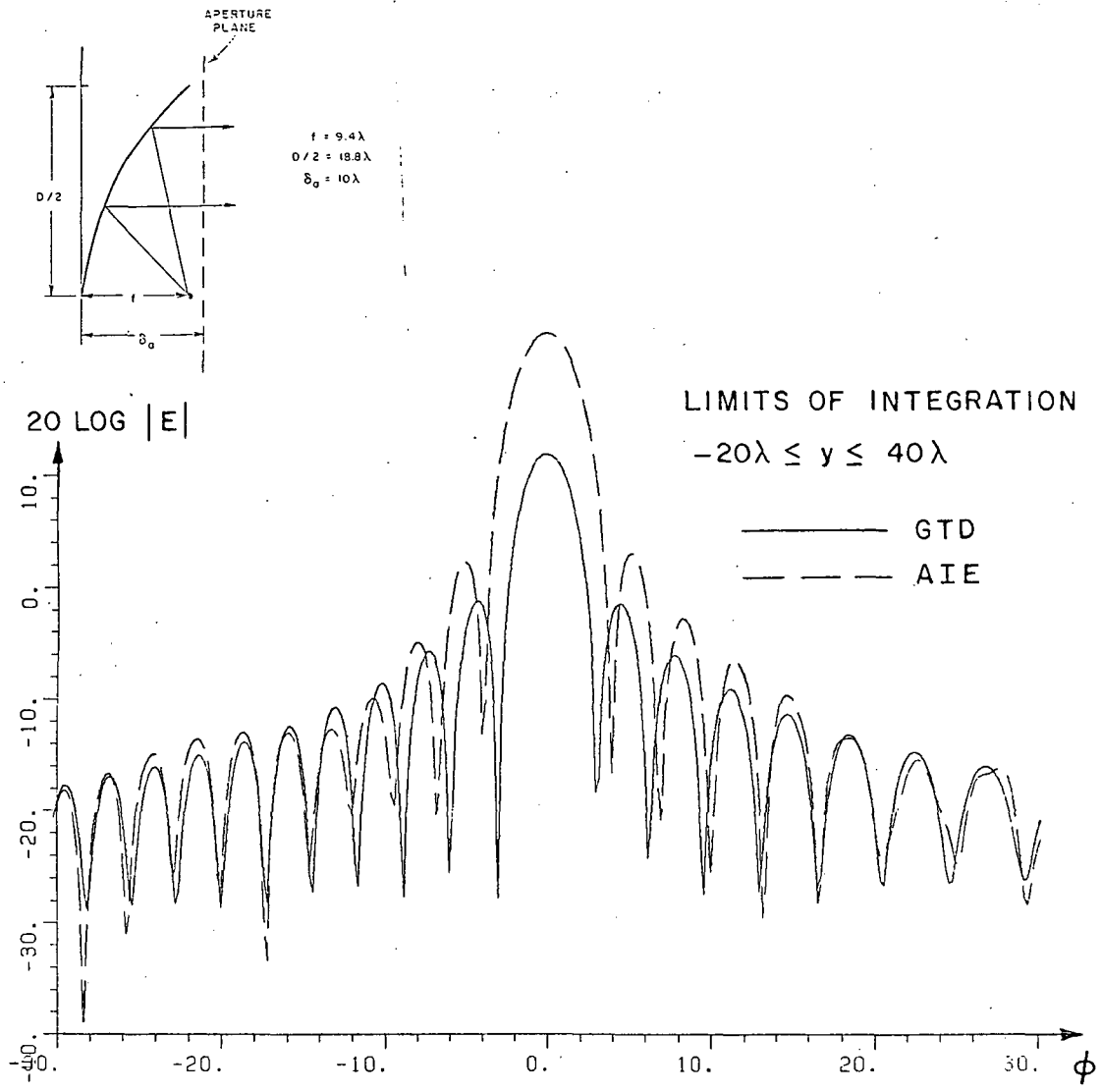

Figure 8.5 Far field radiation pattern with nonuniform aperture illumination. AIE solution.

CHAPTER IX

CONCLUSIONS

The method of extended aperture integration (AIE) is useful when the more conventional AI and GTD solutions do not overlap. Otherwise, it is best avoided because of the additional integration required.

Based on this study, AIE seems to give good results for the first four or five sidelobes with only a moderate extension of the aperture plane. Little is gained by integrating the aperture field beyond the extent of its transition regions. The convergence of the AIE solution to the correct result is extremely slow, past the fourth or fifth sidelobe. It is not a good way to calculate far out sidelobes.

Strictly speaking, the aperture plane must not get too close to the reflector, because GTD may not be valid there. In practice, however, the aperture plane may be moved right up to the reflector. Any errors in the edge diffraction calculations will average out in the integration process, and will not affect the final result. This is useful because the extent of the aperture field transition regions may be minimized by moving the aperture plane as close as possible to the reflector rim. This minimizes the amount of additional integration necessary. However,

the aperture plane should remain perpendicular to the main beam of the antenna.

The AI solution works best for a reflector with a highly tapered feed. With little edge illumination, geometrical optics does quite well in approximately the aperture field. On the other hand, a feed taper increases the extent of the caustic region - a situation highly unfavorable for the GTD solution. We see that favorable conditions for both solutions are mutually exclusive. Because of this, the angle at which we can switch over from an AI or AIE solution to a GTD solution will increase as feed taper increases.

Although this work only treats the special case of a parabolic reflector, AIE may be used for any aperture antenna.

A planar aperture was used in this study because it facilitates application of image theory. The free space Green's function may then be used in the radiation integral to obtain the radiation pattern. Another possible approach would be to completely enclose the antenna by a surface, and calculate both $\overline{J}_S$ and $\overline{M}_S$ over the entire surface. Integrating these currents would give the radiation pattern anywhere outside the surface. Such an approach would be interesting, but probably not advantageous, because GTD with AI or AIE can be used to calculate the complete radiation pattern.

In a realistic three dimensional problem, vertex diffractions would have to be included in AIE aperture field calculations. Its validity in the extreme near field would have to be investigated. Based on the promising results in two dimensions, further investigations in 3-D seem worthwhile.

APPENDIX A

RADIATION INTEGRALS

For an $\hat{\ell}$ directed electric current as in Figure A.1, we have

$$dH_z = \hat{z} \cdot (\hat{\ell} x \hat{\rho})\ (-jk/4)\ J_\ell\ H_1^{(2)}\ d\ell \quad .$$

Using the large argument from of $H_1^{(2)}$ and integrating,

$$H_z = \sqrt{\frac{k}{8\pi}} \int_{\substack{\text{all} \\ \text{currents}}} \hat{z} \cdot (\hat{\ell} x \hat{\rho})\ J_\ell\ \frac{e^{-jk\rho}}{\sqrt{\rho}}\ d\ell \quad . \tag{A.1}$$

By duality, an $\hat{\ell}$ directed magnetic current radiates as

$$E_z = \sqrt{\frac{k}{8\pi}} \int_{\substack{\text{all} \\ \text{currents}}} \hat{z} \cdot (\hat{\ell} x \hat{\rho})\ M_\ell\ \frac{e^{-jk\rho}}{\sqrt{\rho}}\ d\ell \quad . \tag{A.2}$$

For a $\hat{z}$ directed electric current as in Figure A.2, we have

$$dE_z = -kZ_o/4\ J_z\ H_o^{(2)}(k\rho)d\ell \quad .$$

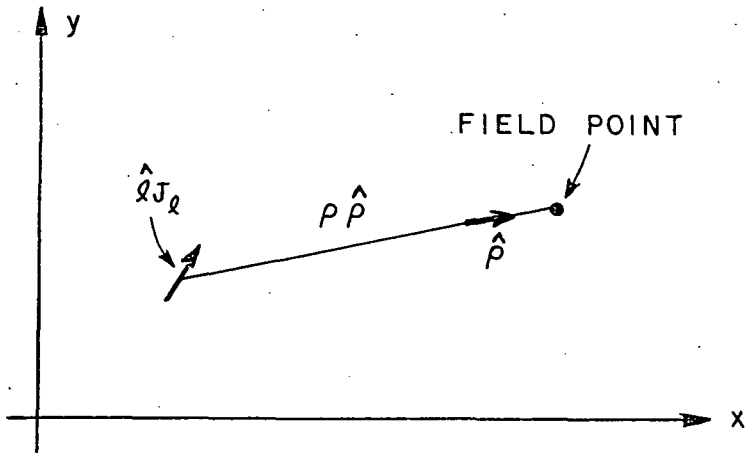

Figure A.1. An $\hat{\ell}$ directed current element.

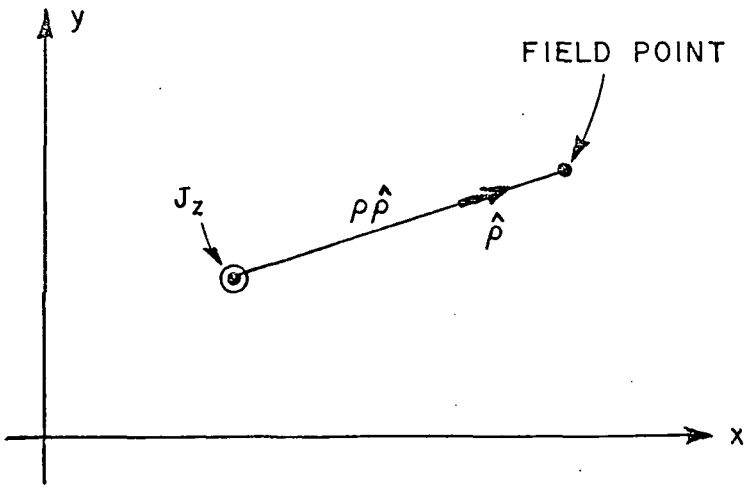

Figure A.2. A $\hat{z}$ directed current element.

Using the large argument form of $H_0^{(2)}$ and integrating,

$$E_z = -Z_o\sqrt{\frac{k}{8\pi}}\; e^{j\pi/4} \int_{\substack{\text{all}\\ \text{currents}}} J_z \frac{e^{-jk\rho}}{\sqrt{\rho}}\, d\ell \quad . \tag{A.3}$$

By duality, a $\hat{z}$ directed magnetic current radiates as

$$H_z = -Y_o\sqrt{\frac{k}{8\pi}}\; e^{j\pi/4} \int_{\substack{\text{all}\\ \text{currents}}} M_z \frac{e^{-jk\rho}}{\sqrt{\rho}}\, d\ell \quad . \tag{A.4}$$

APPENDIX B

GEOMETRICAL OPTICS IN TWO DIMENSIONS

The material here is taken from [2].

For a perfectly conducting surface as shown in Figure B.1, with radius of curvature R, the E or H field may be found from its value at Q:

$$E_z(\ell_s) = E_z(Q)\sqrt{\frac{\rho^r}{\rho^r+\ell_s}}\, e^{-jk\ell_s} \quad \text{, and}$$

$$H_z(\ell_s) = H_z(Q)\sqrt{\frac{\rho^r}{\rho^r+\ell_s}}\, e^{-jk\ell_s} \qquad (B.1)$$

where the caustic distance of reflection ρ^r is given by

$$\frac{1}{\rho^r} = \frac{1}{\ell_i} + \frac{2}{R\cos\theta^i} \quad . \qquad (B.2)$$

R is the radius of curvature for the surface at Q, and θ^i is the angle between the incident ray and the surface normal vector at Q.

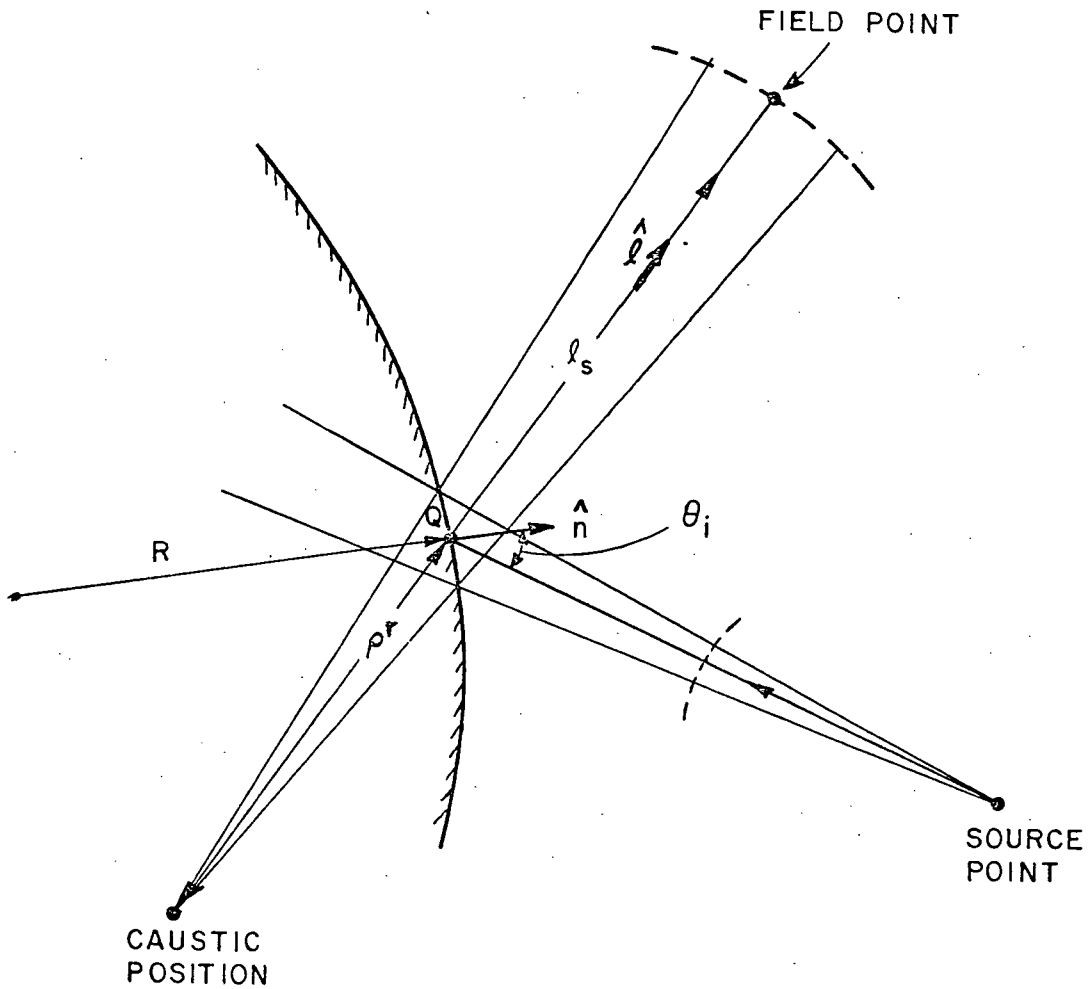

Figure B.1 Reflection from a curved surface.

The electric and magnetic fields are related by

$$\overline{E} = Z_c \, \overline{H} \times \hat{\ell} \quad .$$

Since the tangential electric field vanishes at the perfectly conducting surface,

$$E_z(Q) = -E_z^{inc}(Q) \qquad \text{and}$$

$$H_z(Q) = H_z^{inc}(Q) \quad . \tag{B.3}$$

APPENDIX C

GTD FOR A PERFECTLY CONDUCTING WEDGE

The material here is taken from [2].

The high frequency solution for the fields diffracted by the edge shown in Figure C.1 is known. Either face may be concave or convex. The formulation is valid for any wedge angle WA = $(2-n)\pi$. We shall only need the half plane case (n=2), with the "o" face concave and the "n" face approximately flat.

The solution is [2]

$$E_z^d(\bar{\rho}) = E_z^{inc}(\bar{\rho})\, D_s(\bar{\rho},\bar{\rho}')\, \frac{e^{-jk\rho}}{\sqrt{\rho}} \tag{C.1}$$

$$H_z^d(\bar{\rho}) = H_z^{inc}(\bar{\rho})\, D_h(\bar{\rho},\bar{\rho}')\, \frac{e^{-jk\rho}}{\sqrt{\rho}} \tag{C.2}$$

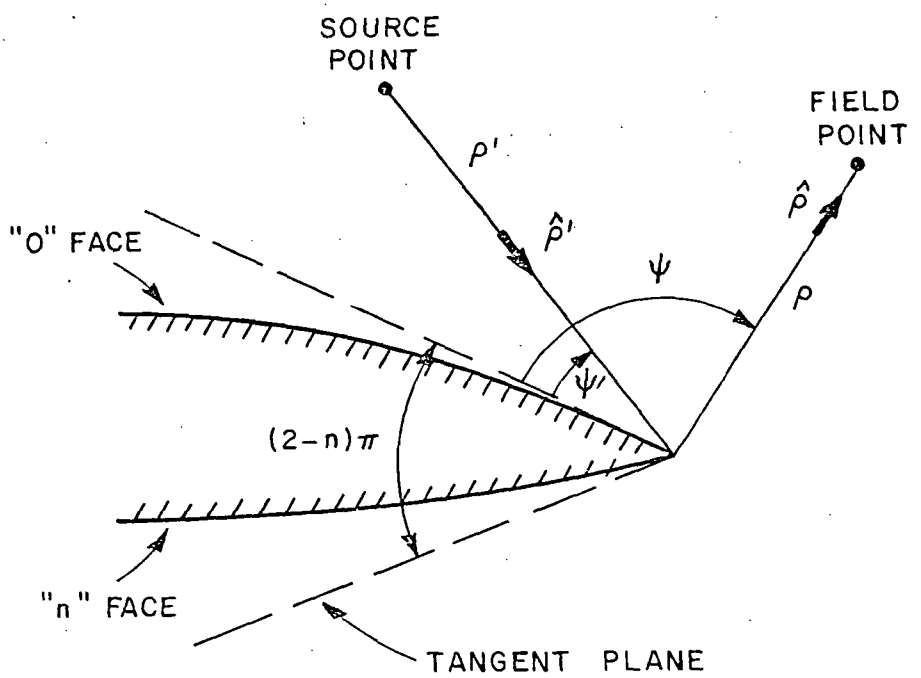

Figure C.1 Diffraction by a wedge with curved faces.

where

$$D_{s \atop h} = \frac{-e^{-j\pi/4}}{2n\sqrt{2\pi k}}\left[\cot\left(\frac{\pi+(\psi-\psi')}{2n}\right)F(kL^{in}a^{+}(\psi-\psi')+\cot\left(\frac{\pi-(\psi-\psi')}{2n}\right)F(kL^{io}a^{-}(\psi-\psi'))\right.$$

$$\left. \mp \left\{ \cot\left(\frac{\pi+(\psi+\psi')}{2n}\right)F(kL^{rn}a^{+}(\psi+\psi')+\cot\left(\frac{\pi-(\psi+\psi')}{2n}\right)F(kL^{ro}a^{-}(\psi+\psi'))\right\}\right] . \tag{C.3}$$

The "L" parameters of $D_{s,h}$ are chosen to correctly compensate for any discontinuities in the incident and reflected fields. With a cylindrical wave as the incident field, we have

$$L^{io} = L^{in} = \frac{\rho\rho'}{\rho+\rho'} \tag{C.4}$$

$$L^{ro} = \frac{\rho\rho_{co}}{\rho+\rho_{co}} \tag{C.5}$$

$$L^{rn} = \frac{\rho\rho_{cn}}{\rho+\rho_{cn}} \tag{C.6}$$

where ρ_{co} and ρ_{cn} are the caustic distances of reflection for fields reflected from the "o" face and "n" face, respectively. They are constants, and take on the values given by Equation (B.2) at the reflection boundaries. This is unlike the caustic ρ^r for the reflected field, which varies with the aspect of the observer.

The general form of $a^{\pm}(\psi\pm\psi')$ involves a fairly long description [2]. It is a measure of the angular separation between the field point, and a reflection boundary, or incident shadow boundary.

However, for the case of a half plane (n=2) it is simply

$$a^{+}(\psi\pm\psi') = a^{-}(\psi\pm\psi') = a(\psi\pm\psi') \quad \text{where}$$

$$a(\psi\pm\psi') = 2\cos^2\left(\frac{\psi\pm\psi'}{2}\right) \quad . \tag{C.7}$$

The "transition function" F is given by

$$F(x) = 2j\sqrt{x}\, e^{jx} \int_{\sqrt{x}}^{\infty} e^{-j\tau^2}\, d\tau \quad . \tag{C.8}$$

In the far field, $F(x)\to 1$ and the solution reduces to Keller's results [4].

For our purposes, this completes the discussion of edge diffracted fields.

APPENDIX D

METHOD OF STATIONARY PHASE

The material here is taken from [3].

We wish to evaluate integrals of the type

$$I = \int_a^b F(y)e^{jkf(y)}dy \tag{D.1}$$

where F is the magnitude, and f is the phase of the integrand. If F(y) is much more slowly varying than f(y), and k is large, the integrand will appear as in Figure D.1. Then, [3] shows that

$$I \sim F(y_s)\sqrt{\frac{2\pi}{k|f''(y_s)|}}\, e^{j[kf(y_s)+(\pi/4)\mathrm{sgn}(f''(y_s))]} \tag{D.2}$$

$$+ \frac{1}{k}\,\frac{F(y=a)}{f'(y=a)}\, e^{j[kf(a)-\pi/2]}$$

$$+ \frac{1}{k}\,\frac{F(y=b)}{f'(y=b)}\, e^{j[kf(b)-\pi/2]}$$

where $f'(y_s)=0$, i.e., y_s is the stationary phase point.

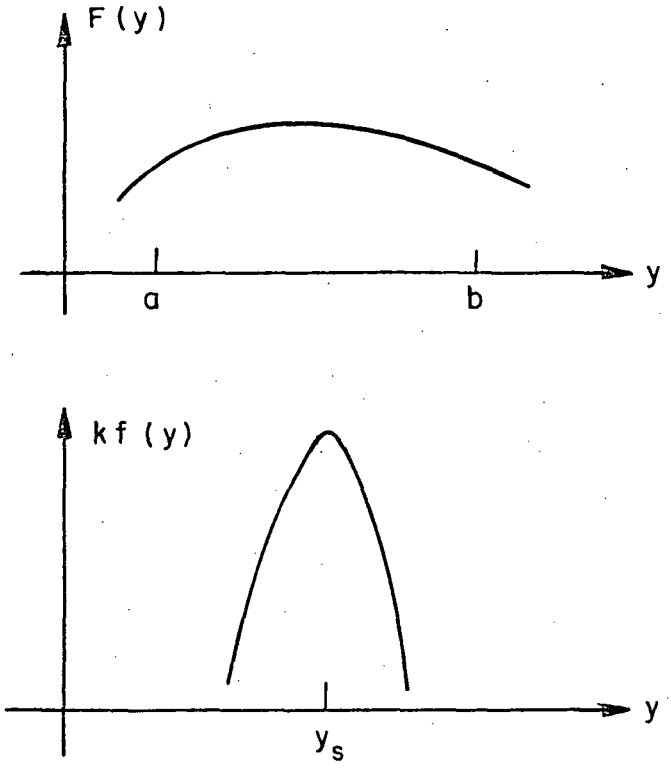

Figure D.1 Typical behavior of the integrand, magnitude and phase.

The first term of Equation (D.2) is the stationary phase contribution, whereas the second two terms are endpoint contributions. It has been assumed that the endpoints "a" and "b" are not near the stationary point y_s.

BIBLIOGRAPHY

[1] R.F. Harrington, Time Harmonic Electromagnetic Fields, McGraw-Hill, 1961.

[2] R.G. Kouyoumjian, P.H. Pathak, and W.D. Burnside, "A Uniform GTD for the Diffraction by Edges, Vertices, and Convex Surfaces", to appear in Theoretical Methods for Determining the Interaction of Electromagnetic Waves with Structures, Ed. J.K. Skwirzynski, by Sijthoff and Noordhoff, Netherlands.

[3] L.B. Felsen and N. Marcuvitz, Radiation and Scattering of Waves, Prentice-Hall, New Jersey, 1973.

[4] J.B. Keller, "Geometrical Theory of Diffraction", J. Opt. Soc. Am. 52, pp. 116-130, 1962.

[5] T.S. Chu and R.H. Turrin, "Depolarization Properties of Offset Reflector Antennas", IEEE Trans. on Antennas and Propagation, 21, pp. 339-345, May 1973.

[6] R.C. Rudduck and S.H. Lee, "Numerical Electromagnetics Code (NEC) Reflector Antenna Code; Part I: User's Manual", Report 784508-19, September 1979, The Ohio State University ElectroScience Laboratory, Department of Electrical Engineering; prepared under Contract N00123-76-C-1371 for Naval Regional Procurement Office, Long Beach, California.

[7] R.C. Rudduck and S.H. Lee, "Numerical Electromagnetic Code (NEC) - Reflector Antenna Code. Part II: Code Manual", Report 784508-16, September 1979, The Ohio State University ElectroScience Laboratory, Department of Electrical Engineering; prepared under Contract N00123-76-C-1371 for Naval Regional Procurement Office, Long Beach, California.